The Astrophysical Journal, 841:50 (20pp), 2017 May 20 https://doi.org/10.3847/1538-4357/aa6d78

High-resolution Optical Spectroscopic Observations of Four Symbiotic Stars: AS 255, MWC 960, RW Hya, and StHα 32*

C. B. Pereira[1], N. O. Baella[2,3], N. A. Drake[1,4], L. F. Miranda[5], and F. Roig[1]
[1] Observatório Nacional/MCTIC, Rua Gen. José Cristino 77, Rio de Janeiro, 20921-400, Brazil; claudio@on.br, drake@on.br, froig@on.br
[2] Unidad de Astronomía, Instituto Geofísico del Perú, Lima, Perú; nobar.baella@gmail.com
[3] Departamento de Ciencias, Sección Física, Pontificia Universidad Católica del Perú, Apartado 1761, Lima, Perú
[4] Laboratory of Observational Astrophysics, Saint Petersburg State University, Universitetski pr. 28, 198504, Saint Petersburg, Russia
[5] Instituto de Astrofísica de Andalucía - CSIC, C/Glorieta de la Astronomía s/n, E-18008 Granada, Spain; lfm@iaa.es
Received 2017 January 24; revised 2017 April 7; accepted 2017 April 14; published 2017 May 23

Abstract

We report on the analysis of high-resolution optical spectra of four symbiotic stars: AS 255, MWC 960, RW Hya, and StHα32. We employ the local-thermodynamic-equilibrium model atmospheres of Kurucz and the spectral analysis code MOOG to analyze the spectra. The abundance of barium and carbon was derived using the spectral synthesis technique. The chemical composition of the atmospheres of AS 255 and MWC 960 show that they are metal-poor K giants with metallicities of −1.2 and −1.7 respectively. StHα32 is a CH star and also a low-metallicity object (−1.4). AS 255 and MWC 960 are yellow symbiotic stars and, like other previously studied yellow symbiotics, are *s*-process enriched. StHα32, like other CH stars, is also an *s*-process and carbon-enriched object. RW Hya has a metallicity of −0.64, a value in accordance with previous determinations, and is not *s*-process enriched. Based on its position in the 2MASS diagram, we suggest that RW Hya is at an intermediate position between yellow symbiotics and classical S-type symbiotics. We also discuss whether the dilution effect was the mechanism responsible for the absence of the *s*-process elements overabundance in RW Hya. The luminosity obtained for StHα32 is below the luminosity of the asymptotic giant branch (AGB) stars that started helium burning (via thermal pulses) and became self-enriched in neutron-capture elements. Therefore, its abundance peculiarities are due to mass transfer from the previous thermally pulsing AGB star (now the white dwarf) that was overabundant in *s*-process elements. For the stars AS 255 and MWC 960, the determination of their luminosities was not possible due to uncertainties in their distance and interstellar absorption. AS 255 and MWC 960 have a low galactic latitude and could be bulge stars or members of the inner halo population. The heavy-element abundance distribution of AS 255 and MWC 960 is similar to that of the other yellow symbiotics previously analyzed. Their abundance patterns follow that of the thick disk population for RW Hya and of the halo population for AS 255, MWC 960, and StHα32. We also determined the rotational velocities of these four symbiotic stars and compare our results with those of single field stars.

Key words: binaries: symbiotic – stars: abundances – stars: chemically peculiar – stars: evolution

1. Introduction

The nature of symbiotic stars seems to be well established nowadays: they are interacting binaries formed by a red giant and a hot source (white dwarf) ionizing the wind of the cool component. In the visible, the spectrum is dominated by emission lines that originated from the nebula and the giant's continuum characterized by strong TiO absorption features. In addition, the division of symbiotic stars into two basic classes according to their emission is also well established: D- and S-type symbiotic stars. Those presenting continuum emission between 1.0 and 5.0 μm are D-type since the continuum emission is attributed to dust, and those showing a stellar spectrum in the same spectral range are S-type.

Following these two different classes, other physical properties of the symbiotic binaries further corroborate the separation between the S- and the D-type symbiotics, such as orbital period and electron density of the ionized nebulae. In addition, the distinction in the infrared is also related to the different evolutionary states of the cool stars in the symbiotic systems: in the D-types, the cool component is a Mira M-type star (or in a few cases a carbon star) while in the S-type the cool component is also an M-type star, but of the luminosity class III. The differences between the S- and D-types were defined after several photometric surveys of emission line objects, carried out in the infrared using J, H, K, and L filters (Allen & Glass 1974, 1975).

Most symbiotic stars are of S-type. They comprise 80% of the total number of known symbiotics (Belczyński et al. 2000). However, there is a small subsample of S-type symbiotic stars for which the cool component is warmer than an M-type, which is typically of mid-K spectral type (Mürset & Schmid 1999). Schmid & Nussbaumer (1993) classified them as yellow symbiotics, with an effective temperature of typically $4000\,\mathrm{K} \leqslant T_{\rm eff} \leqslant 7000\,\mathrm{K}$, regardless of their infrared types. Therefore, according to these authors, yellow symbiotics are both mid-K S-type symbiotic stars as well as the warm giants of the D′-type systems. D′-type systems, first introduced by Allen (1982), also present, like the D-types, an infrared excess. The cool stars of these binary systems have F–G spectral types (Schmid & Nussbaumer 1993).

Since symbiotic stars are binary systems, the investigation and analysis of their absorption spectra may reveal whether mass transfer has happened in these systems in the past. Through measuring the abundance of some key elements, such

* Based on the observations made with the 2.2 m telescope at the European Southern Observatory (La Silla, Chile) under agreement between ESO and Observatório Nacional/MCTI.

as elements created by the slow neutron-capture reactions (*s*-process), one may probe their overabundances. Because these symbiotics are not luminous enough to have undergone the third dredge-up in the AGB phase (Pereira & Roig 2009), the overabundances of the *s*-process elements have been attributed to the mass transfer in the binary system from a former AGB star (now a white dwarf in the system).

In this paper, we extend the study already done for the yellow symbiotic stars BD-21°3873, Hen 2-467 and CD-43° 14304, Hen 3-863, Hen 3-1213, and StHα176 based on high-resolution optical spectroscopy (Pereira & Porto de Mello 1997; Pereira et al. 1998; Pereira & Roig 2009) to another two yellow symbiotic stars, AS 255 and MWC 960, one CH symbiotic star StHα32, and to RW Hya (an M-type symbiotic star), which is considered a red symbiotic star, with the aim of deriving the atmospheric parameters and chemical composition of the late-type components of these systems. AS 255 and MWC 960 have already been classified as K4 and K7 giants, respectively, by Mürset & Schmid (1999), and StHα32 was classified as a CH star by Schmid (1994). RW Hya is a well known red symbiotic star (those with spectral types later than M0, Belczyński et al. 2000). We will show that AS 255, MWC 960, and StHα32 are metal-poor and *s*-process enriched stars, thus adding these objects to the sample of the *s*-process enriched symbiotic stars already studied through high-resolution spectroscopy. RW Hya is also a metal-poor object in agreement with the results based on high-resolution infrared spectroscopy obtained by Mikolajewska et al. (2014). This makes RW Hya an interesting target to search for *s*-process element lines. Being a low-metallicity object, the spectrum of RW Hya is not severely crowded by the TiO molecular bands if RW Hya was a solar metallicity star. Therefore, if the cool component of RW Hya was polluted by a thermally pulsing asymptotic giant branch (TP-AGB) star, and considering that the efficiency of the *s*-process is anti-correlated with metallicity, one would be able to detect and to measure such overabundances, if they are present.

2. Observations

The high-resolution spectra of AS 255, MWC 960, RW Hya, and StHα32 were obtained with the FEROS (Fiberfed Extended Range Optical Spectrograph) echelle spectrograph (Kaufer et al. 1999) at the 2.2 m ESO telescope at La Silla (Chile), during the nights of 2009 May 12, (AS 255), 2009 May 14 (RW Hya), 2008 August 18 (MWC 960), and 2008 December 23 (StHα32). For AS 255, MWC 960, and StHα32, two exposures of 3600 s each were obtained. For RW Hya, an exposure of 2700 s was obtained. Technical details about the FEROS spectrograph are given in Santrich et al. (2013). Figure 1 shows sample spectra of the program stars.

3. Analysis and Results

3.1. Line Selection, Measurement, and Oscillator Strengths

Several atomic absorption lines used in this study are basically the same as those used by Pereira & Roig (2009) in the analysis of photospheric abundances of S-type yellow symbiotic stars. The atomic data for Fe I and Fe II lines, that is the lower excitation potentials (χ (eV)) of the transitions and the log-*gf* values, were taken from Lambert et al. (1996) and Castro et al. (1997). Table 1 shows our measurements.

3.2. Determination of the Atmospheric Parameters

The determination of the stellar atmospheric parameters, such as effective temperature ($T_{\rm eff}$), surface gravity ($\log g$), microturbulence (ξ), and metallicity ([Fe/H]) (we use the notation $[{\rm X/H}] = \log(N_{\rm X}/N_{\rm H})_{\star} - \log(N_{\rm X}/N_{\rm H})_{\odot}$) were done in the same way as in Pereira & Roig (2009). In brief, it consists of using the local thermodynamic equilibrium (hereafter LTE) model atmospheres of Kurucz (1993) and the spectral analysis code MOOG (Sneden 1973). Details of such determinations are also given in Pereira & Roig (2009). Table 2 shows the final adopted atmospheric parameters. We found typical uncertainties of the temperature, gravity, and microturbulent velocity of $\sigma(T_{\rm eff}) = \pm$100–130 K, $\sigma(\log g) = \pm$0.2–0.3, $\sigma(\xi) = \pm$0.2–0.3 km s^{-1}, and σ([Fe/H]) = ±0.13–0.18.

In M-type stars, the traditional methods to determine the gravity, using the ionization equilibrium, which requires that neutral and ionized lines provide the same abundance, face two difficulties. The first one is related to the presence of strong TiO absorption bands. These molecular bands cause severe blanketing in the visual spectra of these kinds of stars, thus causing several neutral and ionized atomic lines to be blended, which complicates not only the measurements of equivalent widths but also the continuum placement. Therefore, some spectral windows should be selected that are free of strong molecular opacities. In the optical spectra, there is a region between 7400 Å and 7600 Å that has been used by Smith & Lambert (1985) and Vanture & Wallerstein (2002) to select some atomic lines of some elements for the determination of their abundances. The second difficulty is the absence or weakness of Fe II lines, which makes the application of the ionization equilibrium impossible due to the low effective temperature of an M-type star, especially for the later spectral types.

However, during the inspection of the spectrum of the RW Hya, it has been noticed that not only did the spectrum not seem to be very crowded by the several rotational lines due to the TiO molecule but also that some neutral absorption lines seemed to be weakened for a star at this temperature. In fact, and as can be seen in Table 2, the observed weakening of some absorption lines is due to the low metallicity found for RW Hya. Thus, thanks to the low metallicity of RW Hya, we were able to measure several Fe I and a few Fe II lines in its spectrum, allowing us to determine the spectroscopic gravity. We also note that more spectral regions, besides those in the 7400 Å and 7600 Å wavelength range, have been used.

Considering the date of observation of RW Hya, the orbital phase is 0.7 following the ephermeris given in Belczyński et al. (2000). According to Gromadzki et al. (2013), at this phase, the star has its maximum brightness, suggesting that possible veiling effects could be present in the spectrum of RW Hya. It is also worth mentioning that the metallicity derived for RW Hya based on optical spectroscopy (-0.64 ± 0.14, this work) is similar to the metallicity of -0.76 ± 0.06 based on infrared observations (Mikolajewska et al. 2014). If veiling effects were present in RW Hya, the metallicity obtained from optical observations would be different from that based on infrared ones. In addition, other recent high-resolution spectroscopic observations in the infrared further support the absence of veiling in stars similar to RW Hya, since they confirm previuos results obtained with high-resolution optical spectroscopy, as in the cases of CD-43°14304 (-1.15 ± 0.19, Pereira & Roig 2009; -1.03 ± 0.07, Galan et al. 2017) and Hen 3-1213

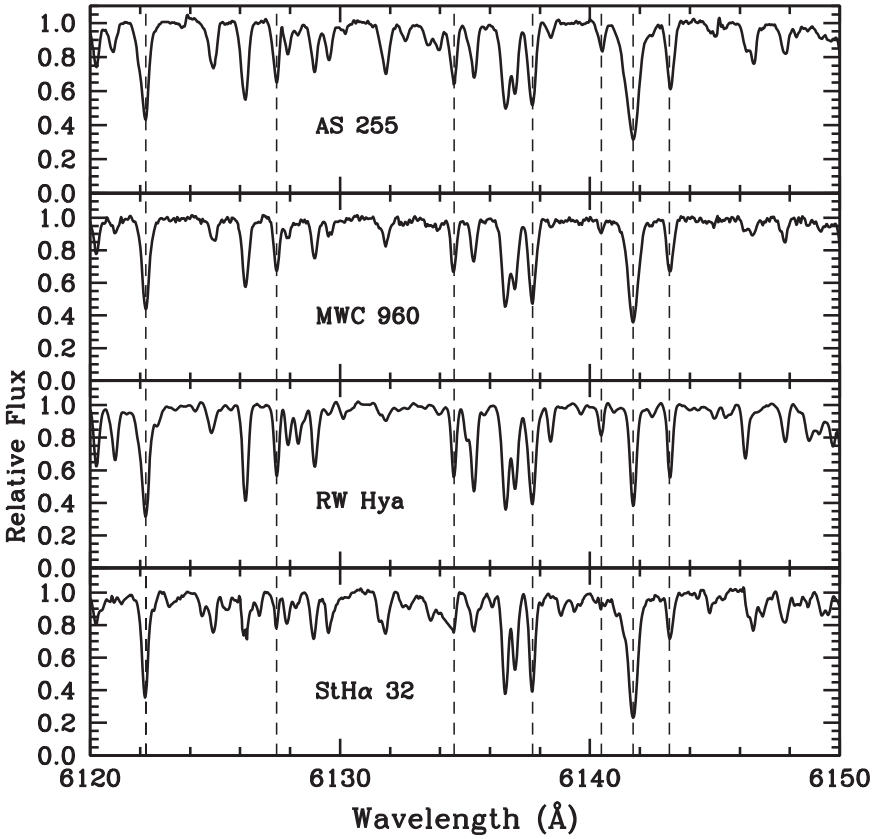

Figure 1. Sample spectra of the yellow symbiotic stars AS 255 and MWC 960, the M-type symbiotic RW Hya, and the carbon symbiotic StHα32 analyzed in this work. Dotted vertical lines show the transitions of Ca I 6122.23 Å, Zr I 6127.48 Å, Zr I 6134.57 Å, Fe I 6137.70 Å, Zr I 6140.46 Å, Ba II 6141.73 Å, and Zr I 6143.18 Å.

(-0.93 ± 0.16; Pereira & Roig 2009; -0.68 ± 0.08, Galan et al. 2016). Table 2 presents the two previous atmospheric parameter determinations for RW Hya by Mikolajewska et al. (2014) and by Schild et al. (1996). Schild et al. (1996) did not obtain the spectroscopic gravity based on ionization equilibrium, but from their results for the mass and the radius of the cool component, their value shows a good agreement with our result.

We also note that the radial velocity of Hen 3-1213 was mistakenly given in Table 3 of Pereira & Roig (2009) as $+46$ km s^{-1}, while the correct value is -46 km s^{-1}, as given in Table 2 of this work.

3.3. Spectral Types and Infrared Color Indexes

The cool components of AS 255 and MWC 950 were classified by Mürset & Schmid (1999) as $\leqslant$K 4 and K 7 stars, respectively, based on their optical and near-infrared spectra. AS 255 was also investigated by Medina Tanco & Steiner (1995). These authors classified it as a K 3 star obtaining an effective temperature of 4256 K based on the TiO index, which is in good agreement with our derived value. StHα32 was classified as a CH star, by Schmid (1994) and, therefore, is a metal-poor candidate halo star with a high radial velocity (Schmid & Nussbaumer 1993). Based on the strengths of some absorption features, Schmid (1994) estimated an effective temperature of $\sim$4300 K, the same value obtained in this work. RW Hya is the best studied object of our study. It was classified as an M-type symbiotic star with a spectral type M 2 (Mürset & Schmid 1999; Belczyński et al. 2000). Schild et al. (1996), based on high-resolution spectroscopy, obtained the effective temperature, radius, and mass of the red giant in RW Hya. Mikolajewska et al. (2014), using high-resolution infrared spectroscopy, also derived atmospheric parameters and photospheric abundances of the red giant of this system.

Table 2 also lists the photometric indexes $(J-K)$ and $(H-K)$ corrected for reddening of the yellow symbiotic stars analyzed here and of others in previous works. Reddening was estimated using the Galactic Dust Reddening and Extinction Service of IRSA (Infrared Science Archive: http://irsa.ipac.caltech.edu/applications/DUST/) to obtain the "E(B-V) Reddening" values, and convert the $E(B-V)$ to $A(J)$, $A(H)$, and $A(Ks)$ extinctions using the relationships given by Bilir et al. (2008). The value given by IRSA should be viewed with caution because it represents the total Galactic visual extinction for a line of sight. Since yellow symbiotic stars have similar photometric indexes $(J-K)$ and $(H-K)$, we should also expect similar effective temperatures for all of these stars, as seen in Table 2.

In Figure 2, we show the position of the studied stars in the 2MASS $(J-H)$ versus $(H-K_s)$ diagram. We see that AS 255 and MWC 960 are in the same region occupied by yellow symbiotic stars. StHα32 also displays similar characteristics as the yellow symbiotic stars (low metallicity and high radial velocity), and, albeit being a CH star, its position in the 2MASS diagram is similar to that of the yellow symbiotics. RW Hya displays an interesting position in the diagram. It occupies a region that seems to be the limit for the classical S-type symbiotics approaching to the region of the yellow symbiotic stars.

Table 1
Observed Fe I and Fe II Lines

Element	λ	χ(eV)	log gf	Equivalent widths (mÅ)			
				AS 255	MWC 960	RW Hya	StHα 32
Fe I	5125.12	4.22	−0.08	⋯	106	⋯	⋯
	5159.06	4.28	−0.65	⋯	72	⋯	⋯
	5162.27	4.18	+0.08	⋯	98	⋯	⋯
	5242.49	3.63	−0.97	125	99	⋯	101
	5288.52	3.69	−1.51	⋯	59	⋯	54
	5307.36	1.61	−2.97	⋯	⋯	⋯	150
	5322.04	2.28	−2.84	⋯	122	137	110
	5364.87	4.45	+0.23	⋯	93	⋯	112
	5369.96	4.37	+0.54	⋯	⋯	⋯	131
	5373.71	4.47	−0.71	85	57	⋯	56
	5389.48	4.42	−0.25	⋯	88	99	108
	5400.50	4.37	−0.10	141	⋯	⋯	⋯
	5441.34	4.31	−1.58	⋯	⋯	55	⋯
	5445.04	4.39	0.04	112	91	⋯	⋯
	5554.90	4.55	−0.38	103	62	⋯	⋯
	5560.21	4.43	−1.04	47	29	63	⋯
	5567.39	2.61	−2.56	119	99	⋯	120
	5569.62	3.42	−0.49	⋯	138	⋯	⋯
	5576.09	3.43	−0.85	⋯	122	⋯	131
	5584.77	3.57	−2.17	⋯	⋯	90	⋯
	5624.02	4.39	−1.33	62	⋯	⋯	⋯
	5633.95	4.99	−0.12	67	34	80	⋯
	5635.82	4.26	−1.74	⋯	⋯	54	⋯
	5638.26	4.22	−0.72	115	70	88	⋯
	5691.50	4.30	−1.37	59	⋯	59	55
	5705.47	4.30	−1.36	42	⋯	⋯	⋯
	5717.83	4.28	−0.98	⋯	⋯	82	⋯
	5731.76	4.26	−1.15	91	48	74	⋯
	5762.99	4.21	−0.41	115	79	120	89
	5791.02	3.21	−2.27	⋯	⋯	⋯	87
	5806.73	4.61	−0.90	42	32	69	⋯
	5916.25	2.45	−2.99	⋯	⋯	106	⋯
	6024.06	4.55	−0.06	118	92	112	⋯
	6027.05	4.08	−1.09	79	55	⋯	63
	6056.01	4.73	−0.40	63	⋯	⋯	53
	6082.71	2.22	−3.58	123	88	⋯	⋯
	6120.25	0.91	−5.95	63	⋯	93	⋯
	6151.62	2.18	−3.29	⋯	107	134	101
	6165.36	4.14	−1.47	⋯	35	⋯	31
	6173.34	2.22	−2.88	⋯	132	⋯	⋯
	6187.99	3.94	−1.57	59	40	⋯	73
	6200.31	2.56	−2.44	126	129	⋯	127
	6213.43	2.22	−2.48	⋯	⋯	⋯	156
	6322.69	2.59	−2.43	122	116	⋯	125
	6411.65	3.65	−0.66	⋯	121	⋯	144
	6518.37	2.83	−2.30	⋯	⋯	⋯	88
	6551.68	0.99	−5.79	⋯	⋯	⋯	42
	6574.23	0.99	−5.02	114	⋯	⋯	97
	6593.87	2.44	−2.42	147	124	⋯	⋯
	6597.56	4.79	−0.92	⋯	⋯	55	⋯
	6608.03	2.28	−4.03	87	⋯	⋯	42
	6609.11	2.56	−2.69	132	106	122	⋯
	6627.55	4.55	−1.68	⋯	⋯	⋯	⋯
	6646.93	2.61	−3.99	⋯	⋯	54	⋯
	6703.57	2.76	−3.16	95	⋯	⋯	⋯
	6739.52	1.56	−4.95	⋯	⋯	⋯	54
	6750.15	2.42	−2.62	132	⋯	⋯	⋯
	6806.85	2.73	−3.21	86	⋯	⋯	⋯
	6810.26	4.61	−0.99	40	⋯	⋯	⋯
	6841.34	4.61	−0.60	⋯	42	⋯	⋯
	6858.15	4.61	−0.93	44	33	71	⋯
	7418.67	4.14	−1.54	⋯	⋯	68	⋯
	7447.43	4.95	−0.97	⋯	⋯	37	⋯

Table 1
(Continued)

Element	λ	χ(eV)	log gf	Equivalent widths (mÅ)			
				AS 255	MWC 960	RW Hya	StHα 32
	7454.02	4.19	−2.43	⋯	⋯	33	⋯
	7507.30	4.44	−0.93	⋯	⋯	83	⋯
	7559.68	5.06	−0.96	⋯	⋯	35	⋯
	7583.98	3.02	−1.97	⋯	⋯	142	⋯
Fe II	4993.35	2.81	−3.67	44	⋯	⋯	53
	5234.62	3.22	−2.24	⋯	⋯	65	81
	5264.81	3.33	−3.12	⋯	23	⋯	⋯
	5284.10	2.89	−3.01	⋯	⋯	⋯	70
	5325.56	3.22	−3.17	⋯	32	⋯	⋯
	5425.25	3.20	−3.21	37	21	23	⋯
	5534.83	3.25	−2.77	⋯	⋯	⋯	54
	5991.37	3.15	−3.56	⋯	21	21	⋯
	6084.10	3.20	−3.80	⋯	⋯	21	⋯
	6149.25	3.89	−2.72	⋯	⋯	⋯	⋯
	6247.55	3.89	−2.34	34	⋯	⋯	52
	6369.46	2.89	−4.19	⋯	⋯	⋯	⋯
	6416.92	3.89	−2.68	28	⋯	⋯	⋯
	6432.68	2.89	−3.58	⋯	⋯	⋯	62
	6456.39	3.90	−2.43	⋯	27	34	⋯

Table 2
Stellar Parameters, Galactic Latitude, Radial Velocities and Derredened Infrared Color Indexes of AS 255, MWC 960, RW Hya, and StHα 32 and of Other Yellow Symbiotics Already Analyzed

Star	T_{eff} (K)	log g	ξ (km s^{-1})	[Fe/H]	l	b	RV km s^{-1}	$(J-H)_0$[a]	$(H-K)_0$[a]
AS 255[b]	4300	1.5	2.5	−1.20	355°	−05°	+278.3 ± 0.5	0.83	0.13
MWC 960[b]	4000	0.5	2.1	−1.72	14°	−08°	−228.7 ± 0.5	0.70	0.20
StHα 32[b]	4300	1.1	2.2	−1.38	197°	−30°	+321.7 ± 1.0	0.69	0.18
RW Hya[b]	3900	0.9	1.5	−0.64	314°	+36°	+7.4 ± 0.2	0.78	0.29
RW Hya[c]	3655	0.5	1.5	−0.76	⋯	⋯	+5.06 → +11.09	⋯	⋯
RW Hya[d]	3770	1.1	⋯	⋯	⋯	⋯		⋯	⋯
AG Dra[e]	4300	1.6	2.3	−1.34	100°	+41°	−147.3 ± 0.4	0.77	0.15
Hen 2-467[f]	4400	1.8	2.3	−1.10	63°	−12°	−106.9 ± 0.5	0.77	0.15
BD-21°3873[g,h]	4300	1.0	2.2	−1.30	327°	+37°	+203.9 ± 0.2	0.76	0.16
Hen 3-863[i]	4300	0.9	1.9	−0.75	305°	+14°	+274	0.88	0.14
StHα 176[i]	4200	0.8	2.0	−1.29	22°	−30°	−24	0.75	0.17
Hen 3-1213[i]	4100	1.1	1.4	−0.93	333°	−02°	−46	0.66	0.01
Hen 3-1213[j]	4100	1.5	2.1	−0.79	⋯	⋯	⋯	⋯	⋯
CD-43°1430[i]	4300	1.6	2.1	−1.15	358°	−41°	+29	0.81	0.22
CD-43°1430[k]	3910	<0.8	⋯	−1.07	⋯	⋯	⋯	⋯	⋯

Notes.
[a] Cutri et al. (2003).
[b] This work.
[c] Mikolajewska et al. (2014).
[d] Schild et al. (1996).
[e] Smith et al. (1996).
[f] Pereira et al. (1998).
[g] Smith et al. (1997).
[h] Pereira & Porto de Mello (1997).
[i] Pereira & Roig (2009).
[j] Galan et al. (2016).
[k] Galan et al. (2017).

3.4. Abundance Analysis

The abundances of chemical elements were determined using the local-thermodynamic-equilibrium (LTE) model-atmosphere techniques already described. We used the line-synthesis code MOOG (Sneden 1973) for the calculations and Table 3 shows the atomic lines used to obtain the abundances of the elements. Tables 4 and 5 give the results, the number of lines employed for each species, *n*, and the standard deviations. Our abundances were

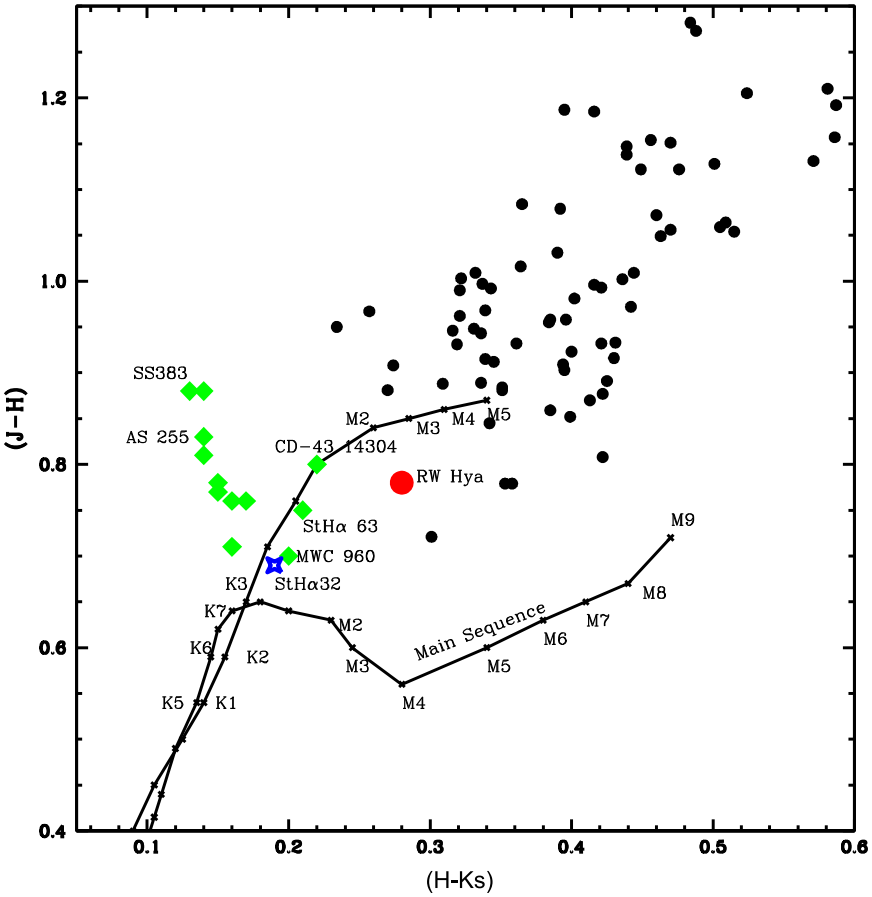

Figure 2. Yellow symbiotic stars and AS 255 and MWC 960 (green diamonds), StHα32 (blue star), and RW Hya (red circle) in the 2MASS color–color diagram. Black circles represent the S-type symbiotics. RW Hya, AS 255, and MWC 960 have been reddening corrected. StHα32 presents a low extinction and was not reddening corrected. We also included the two recently discovered yellow symbiotic stars SS 383 (Baella et al. 2013) and StHα 63 (Baella et al. 2016).

normalized to the solar abundances of Grevesse & Sauval (1998), except iron, for which we adopted log ε(Fe) = 7.52.

For the CH symbiotic star StHα32, we obtained the abundances of carbon and nitrogen, based on the C_2 (0, 1) band head of the Swan system $A^3\Pi_g - X^3\Pi_u$ at 5635 Å and on ^{12}CN lines of the (2, 0) band of the CN red system $A^2\Pi - X^2\Sigma$ in the 7994–8020 Å wavelength range. The oscillator strength of the (0, 2) band $f_{2,0} = 8.4 \times 10^{-4}$ (Sneden & Lambert 1982) was used. Hönl-London factors were calculated using the Schadee (1964) formula. The dissociation energy D_0(CN) = 7.75 eV (Pradhan & Dalgarno 1994) was used. The wavelengths of the ^{12}CN lines were taken from Davis & Phillips (1963) and those of ^{13}CN lines from Wyller (1966). Contamination of the CN features by the telluric H_2O lines was eliminated by dividing our spectra by a high rotating hot star spectrum.

The abundance of oxygen for AS 255 and MWC 960 could not be obtained because the oxygen forbidden line at 6300.31 Å is severely affected by a telluric O_2 line. In StHα32, this oxygen line is too weak to be used for abundance determination, therefore, we assumed [O/Fe] = +0.35 for StHα32. For RW Hya, the oxygen abundance was also not obtained because the oxygen line is strongly affected by the satellite band at λ6174 Å of the TiO absorption $B^3\Pi_2 - X^3\Delta_2$ system.

For StHα32, we determined the ^{12}C/^{13}C isotopic ratio using the same spectral region as that used for the determination of the nitrogen abundance. Figure 3 shows the observed and synthetic spectra of StHα32 in the region around 8002–8007 Å.

The barium abundance for the four stars analyzed in this work was derived using the Ba II line at λ 5853.7 Å. The line data that include hyperfine splitting were taken from McWilliam (1998). Figure 4 shows the observed and synthetic spectra for the four stars around the barium line at λ 5853.7 Å.

3.5. Abundance Uncertainties

The uncertainties of the abundances of the elements for the symbiotic star AS 255 are given in Table 6. Uncertainties in abundances are due primarily to the uncertainties in the temperature, surface gravity, microturbulence velocity, and metallicity and are shown in columns 2 to 5 of Table 6. In addition, uncertainties in abundances due to the uncertainty in equivalent width are shown in column 6. The errors in the equivalent width are set by the S/N ratio and the resolution of the spectra. For a resolution of 48,000 and an S/N equal to 100 and using the expression given in Cayrel (1988), the uncertainty in the equivalent width is approximately 3 mÅ. In column 6, it can be seen that the uncertainty in the abundances of the elements due to the uncertainty in equivalent width is less than the uncertainty due to the atmospheric parameters. The final incertainty in the abundances of the elements were obtained through the calculation of the root squared sum of each uncertainty considering that individual uncertainties are independent.

Table 6 shows that neutral elements are more sensitive to temperature variations, while singly ionized elements are more

Table 3
Other Lines Studied

					Equivalent Widths (mÅ)			
λ	Element	χ(eV)	log gf	Ref	AS 255	MWC 960	RW Hya	StHα32
5682.65	Na I	2.10	−0.70	GS	105	61	150	53
5688.22	Na I	2.10	−0.40	GS	138	89	156	105
6154.22	Na I	2.10	−1.51	R03	⋯	⋯	83	⋯
6160.75	Na I	2.10	−1.21	R03	⋯	25	⋯	⋯
4730.04	Mg I	4.34	−2.39	R03	⋯	57	⋯	⋯
5711.10	Mg I	4.34	−1.75	R99	⋯	120	128	⋯
8712.69	Mg I	5.93	−1.26	WSM	⋯	⋯	36	⋯
8717.83	Mg I	5.91	−0.71	WSM	66	45	76	⋯
8736.04	Mg I	5.94	−0.34	WSM	110	74	100	⋯
5793.08	Si I	4.93	−2.07	R03	46	34	40	⋯
6145.08	Si I	5.62	−1.48	E93	43	⋯	40	35
6155.14	Si I	5.62	−0.77	E93	93	46	⋯	50
8728.01	Si I	6.18	−0.36	E93	⋯	⋯	⋯	26
8742.45	Si I	5.87	−0.51	E93	65	⋯	47	⋯
5581.80	Ca I	2.52	−0.67	C2003	⋯	108	⋯	⋯
5601.29	Ca I	2.52	−0.52	C2003	144	112	⋯	⋯
5857.46	Ca I	2.93	0.11	C2003	143	135	⋯	⋯
5867.57	Ca I	2.93	−1.61	C2003	⋯	38	⋯	⋯
6161.30	Ca I	2.52	−1.27	E93	⋯	104	⋯	⋯
6166.44	Ca I	2.52	−1.14	R03	121	96	⋯	⋯
6169.04	Ca I	2.52	−0.80	R03	132	124	⋯	143
6169.56	Ca I	2.53	−0.48	DS91	⋯	125	⋯	144
6455.60	Ca I	2.51	−1.29	R03	103	66	⋯	119
6471.66	Ca I	2.51	−0.69	S86	⋯	⋯	⋯	129
6499.65	Ca I	2.52	−0.81	C2003	133	⋯	⋯	127
6717.69	Ca I	2.71	−0.52	C2003	158	⋯	⋯	⋯
5113.45	Ti I	1.44	−0.88	E93	⋯	⋯	⋯	58
5219.71	Ti I	0.02	−2.29	MFK	⋯	⋯	⋯	138
5223.63	Ti I	2.09	−0.56	MFK	58	⋯	⋯	21
5295.78	Ti I	1.05	−1.63	MFK	⋯	88	137	54
5503.90	Ti I	2.58	−0.19	MFK	50	34	⋯	⋯
5662.16	Ti I	2.32	−0.11	MFK	94	56	⋯	39
5689.48	Ti I	2.30	−0.47	MFK	54	34	⋯	⋯
5978.55	Ti I	1.87	−0.50	MFK	121	⋯	⋯	84
6091.18	Ti I	2.27	−0.37	R03	⋯	58	104	⋯
6126.22	Ti I	1.05	−1.37	R03	⋯	106	164	⋯
6261.10	Ti I	1.43	−0.48	MFK	⋯	⋯	⋯	125
5084.10	Ni I	3.68	+0.06	E93	⋯	79	⋯	⋯
5010.94	Ni I	3.63	−0.90	MFK	⋯	⋯	⋯	34
5115.40	Ni I	3.83	−0.28	R03	⋯	40	⋯	⋯
5578.73	Ni I	1.68	−2.67	MFK	136	110	⋯	⋯
5587.87	Ni I	1.94	−2.37	MFK	⋯	103	111	⋯
5589.37	Ni I	3.90	−1.15	MFK	⋯	⋯	42	⋯
6086.29	Ni I	4.27	−0.47	MFK	⋯	⋯	42	46
6108.12	Ni I	1.68	−2.49	MFK	⋯	⋯	139	⋯
6128.98	Ni I	1.68	−3.39	MFK	100	⋯	109	80
6130.14	Ni I	4.27	−0.98	MFK	⋯	⋯	⋯	⋯
6176.82	Ni I	4.09	−0.26	R03	83	43	⋯	60
6177.25	Ni I	1.83	−3.60	MFK	52	⋯	⋯	⋯
6327.60	Ni I	1.68	−3.11	MFK	104	95	⋯	⋯
6482.80	Ni I	1.94	−2.63	MFK	93	82	⋯	112
6586.33	Ni I	1.95	−2.81	MFK	85	60	⋯	83
6643.64	Ni I	1.68	−2.03	MFW	⋯	149	⋯	⋯
6767.77	Ni I	1.83	−2.17	MFK	143	139	160	144
6772.32	Ni I	3.66	−0.97	R03	⋯	52	⋯	⋯
7385.24	Ni I	2.72	−1.73	SL85	⋯	84	⋯	⋯
7393.63	Ni I	3.61	+0.03	SL85	⋯	93	116	⋯
7414.51	Ni I	1.99	−1.97	SL85	⋯	⋯	151	⋯
7422.78	Ni I	3.63	−0.30	SL85	114	⋯	120	⋯
7522.78	Ni I	3.66	−0.30	SL85	⋯	93	116	⋯
7525.14	Ni I	3.63	−0.51	SL85	⋯	86	96	⋯
7574.08	Ni I	3.83	−0.49	SL85	⋯	⋯	79	⋯
7788.93	Ni I	1.95	−1.99	E93	⋯	139	⋯	150

Table 3
(Continued)

λ	Element	χ(eV)	log *gf*	Ref	Equivalent Widths (mÅ)			
					AS 255	MWC 960	RW Hya	StHα32
5087.43	Y II	1.08	−0.17	SN96	⋯	⋯	⋯	137
5123.21	Y II	0.99	−0.93	SN96	⋯	108	⋯	⋯
5200.41	Y II	0.99	−0.57	SN96	167	130	⋯	118
5205.72	Y II	1.03	−0.34	SN96	176	130	⋯	118
5289.81	Y II	1.03	−1.85	VWR	89	27	⋯	⋯
5402.78	Y II	1.84	−0.44	R03	125	50	⋯	54
4772.30	Zr I	0.62	−0.06	A04	96	81	⋯	82
4784.94	Zr I	0.69	−0.60	A04	⋯	48	⋯	⋯
4805.87	Zr I	0.69	−0.58	A04	⋯	⋯	⋯	18
4809.47	Zr I	1.58	0.35	A04	50	⋯	⋯	⋯
4815.05	Zr I	0.65	−0.38	A04	62	⋯	⋯	⋯
4828.05	Zr I	0.62	−0.75	A04	43	⋯	⋯	32
5385.13	Zr I	0.52	−0.64	A04	⋯	45	⋯	34
5620.13	Zr I	0.52	−1.09	A04	32	47	⋯	⋯
5879.79	Zr I	0.15	−1.03	A04	⋯	53	⋯	43
5885.62	Zr I	0.07	−1.73	A04	⋯	28	⋯	⋯
5955.34	Zr I	0.00	−1.70	A04	65	50	⋯	⋯
6032.60	Zr I	1.48	−0.35	A04	⋯	12	⋯	⋯
6127.46	Zr I	0.15	−1.06	S96	106	93	108	56
6134.57	Zr I	0.00	−1.28	S96	106	88	111	67
6140.46	Zr I	0.52	−1.41	S96	54	24	43	⋯
6143.18	Zr I	0.07	−1.10	S96	136	108	119	83
6445.72	Zr I	1.00	−0.83	S96	⋯	⋯	28	⋯
7439.89	Zr I	0.54	−1.81	SL85	⋯	⋯	50	⋯
7554.73	Zr I	0.51	−2.28	SL85	⋯	⋯	36	⋯
4934.83	La II	1.25	−0.92	VWR	⋯	⋯	⋯	58
5303.53	La II	0.32	−1.35	VWR	135	76	⋯	⋯
5880.63	La II	0.24	−1.83	VWR	112	74	⋯	119
6320.42	La II	0.17	−1.52	S96	152	105	⋯	⋯
6390.48	La II	0.32	−1.41	VWR	160	102	⋯	⋯
6774.33	La II	0.12	−1.71	VWR	⋯	117	⋯	⋯
4486.91	Ce II	0.30	−0.18	DH	162	⋯	⋯	119
4628.16	Ce II	0.52	+0.14	DH	⋯	132	⋯	⋯
5187.45	Ce II	1.21	+0.17	DH	124	87	⋯	106
5274.24	Ce II	1.28	+0.13	DH	116	84	⋯	113
5330.58	Ce II	0.87	−0.40	DH	99	62	⋯	99
5975.82	Ce II	1.33	−0.45	DH	50	42	⋯	⋯
6043.37	Ce II	1.21	−0.48	DH	71	41	⋯	⋯
6051.80	Ce II	0.23	−1.60	S96	109	70	⋯	⋯
4914.38	Nd II	0.38	−0.70	L09	⋯	102	⋯	142
4987.16	Nd II	0.38	−0.70	L09	⋯	⋯	⋯	118
5063.72	Nd II	0.38	−0.70	L09	⋯	⋯	⋯	109
5092.80	Nd II	0.38	−0.61	L09	153	106	⋯	133
5212.36	Nd II	0.20	−0.96	L09	161	⋯	⋯	⋯
5234.19	Nd II	0.55	−0.51	L09	⋯	126	⋯	⋯
5249.58	Nd II	0.98	+0.20	L09	⋯	113	⋯	126
5255.51	Nd II	0.20	−0.67	L09	160	⋯	⋯	⋯
5306.46	Nd II	0.86	−0.97	L09	104	64	⋯	⋯
5311.46	Nd II	0.98	−0.42	L09	⋯	69	⋯	⋯
5319.81	Nd II	0.55	−0.14	L09	⋯	145	⋯	166
5485.70	Nd II	1.26	−0.12	L09	112	⋯	⋯	102
5740.88	Nd II	1.16	−0.53	L09	91	53	⋯	94
5811.57	Nd II	0.86	−0.86	L09	98	51	⋯	81
7513.73	Nd II	0.92	−1.18	SL85	94	49	17	⋯

Note. A05: Antipova et al. (2004), C2003: Chen et al. (2003), DH : Den Hartog et al. (2003), DS91: Drake & Smith (1991), E93: Edvardsson et al. (1993), GS: Gratton & Sneden (1988), L09: Lawler et al. (2009), MFW: Martin et al. (1988), R03: Reddy et al. (2003), R99: Reddy et al. (1999), SL85: Smith & Lambert (1985), S86: Smith et al. (1986), S96: Smith et al. (1996), SN96: Sneden et al. (1996), VWR: Van Winckel & Reyniers (2000), WSM: Wiese et al. (1969).

sensitive to log *g* variations. For elements with abundances that are based on stronger lines, such as calcium, yttrium, lanthanum, cerium, and neodymium, the error introduced by the microturbulence gives a mean error of 0.14 dex, which is larger than those for other elements with abundances that were derived using weaker lines.

Table 4
Abundances in the Scale of $\log \epsilon(H) = 12.0$ and in the Notation [X/H] and [X/Fe]

	AS 255				MWC 960			
Species	n	log ϵ	[X/H]	[X/Fe]	n	log ϵ	[X/H]	[X/Fe]
Fe I	29	6.32 ± 0.17	−1.20	···	34	5.80 ± 0.14	−1.72	···
Fe II	4	6.31 ± 0.10	−1.21	···	5	5.83 ± 0.11	−1.69	···
Na I	2	5.41	−0.92	+0.28	3	4.71 ± 0.10	−1.62	+0.10
Mg I	2	7.02	−0.56	+0.64	4	6.62 ± 0.09	−0.96	+0.76
Si I	4	7.05 ± 0.19	−0.50	+0.70	3	6.57 ± 0.23	−0.98	+0.74
Ca I	7	5.44 ± 0.14	−0.92	+0.28	9	5.09 ± 0.21	−1.27	+0.45
Ti I	5	4.31 ± 0.12	−0.71	+0.49	7	3.64 ± 0.14	−1.38	+0.34
Ni I	9	5.11 ± 0.19	−1.14	+0.06	16	4.50 ± 0.17	−1.75	−0.03
Y II	4	2.30 ± 0.17	+0.06	+1.26	4	1.20 ± 0.25	−1.04	+0.68
Zr I	10	2.49 ± 0.20	−0.11	+1.09	14	1.67 ± 0.14	−0.93	+0.79
Ba II	1	2.43	+0.30	+1.50	1	1.83	−0.30	+1.42
La II	4	1.81 ± 0.11	+0.64	+1.84	5	0.68 ± 0.13	−0.49	+1.23
Ce II	7	1.90 ± 0.17	+0.32	+1.52	6	1.04 ± 0.19	−0.54	+1.18
Nd II	8	1.99 ± 0.13	+0.49	+1.69	10	1.01 ± 0.18	−0.49	+1.23
[s/Fe] = 1.48; [hs/ls] = 0.46					[s/Fe] = 1.09; [hs/ls] = 0.53			

Table 5
Abundances in the Scale of $\log \epsilon(H) = 12.0$ and in the Notation [X/H] and [X/Fe]

	RW Hya				StHα32			
Species	n	log ϵ	[X/H]	[X/Fe]	n	log ϵ	[X/H]	[X/Fe]
Fe I	28	6.88 ± 0.13	−0.64	···	27	6.14 ± 0.18	−1.38	···
Fe II	4	6.91 ± 0.20	−0.71	···	6	6.14 ± 0.21	−1.38	···
Na I	3	5.84 ± 0.20	−0.49	+0.15	2	5.02	−1.31	+0.07
Mg I	4	7.27 ± 0.18	−0.31	+0.33	···	···	···	···
Si I	3	7.20 ± 0.17	−0.35	+0.23	3	6.73 ± 0.20	−0.82	+0.56
Ca I	···	···	···	···	5	5.60 ± 0.20	−0.76	+0.62
Ti I	3	4.61 ± 0.15	−0.41	+0.23	7	3.88 ± 0.19	−1.14	+0.24
Ni I	14	5.58 ± 0.14	−0.67	−0.03	8	4.96 ± 0.17	−1.29	+0.09
Y II	···	···	···	···	3	1.38 ± 0.10	−0.86	+0.52
Zr I	7	2.11 ± 0.25	−0.49	+0.15	8	2.08 ± 0.18	−0.52	+0.86
Ba II	1	1.51	−0.62	+0.02	1	2.73	+0.60	+1.98
La II	···	···	···	···	2	1.55	+0.38	+1.76
Ce II	···	···	···	···	4	1.58 ± 0.20	0.00	+1.38
Nd II	1	0.93	−0.56	+0.08	9	1.80 ± 0.22	+0.30	+1.68
[s/Fe] = 0.08;					[s/Fe] = 1.36; [hs/ls] = 1.01			

4. Discussion

4.1. The Temperature and Position of RW Hya in the 2MASS Diagram: Is RW Hya a New Yellow Symbiotic Star?

As derived in Section 3.2, the effective temperature of RW Hya is 130–250 K hotter than the two previous estimates given in Table 2. This means that the spectral type of RW Hya, with an effective temperature of 3900 K, can either be K8.6 according to Fluks et al. (1994), which would be the spectral type for a star with an effective temperature of 3895 K, or M0.0 which would be the spectral type for a star with an effective temperature of 3895 K according to Ridgway et al. (1980).

As mentioned in Section 3.3, the position of RW Hya in the color–color diagram is at the border of the region occupied by the classical S-type symbiotic stars and close to the region occupied by the yellow symbiotic stars. Therefore, we conclude that RW Hya may represent an object that is at an intermediate position in the 2MASS diagram between the S-type symbiotics and the yellow symbiotics. To give further support to this conclusion, we mention that the W_{34} index (see Baella et al. 2016 for the definition of this index) of RW Hya has a value of 0.55 that is only 0.01 higher than the corresponding value for SS 383, a yellow symbiotic candidate with a spectral type between K7 and M0 (Baella et al. 2013).

4.2. The Rotational Velocity

We have estimated rotational velocities, $v \sin i$, by means of the spectral synthesis technique using determined atmosphere models. A spectral region with unblended lines was chosen. Synthetic spectra were calculated using a macroturbulent velocity of $3\,\mathrm{km\,s^{-1}}$ and instrumental broadening corresponding to FEROS spectral resolution. Figure 5 shows the observed and

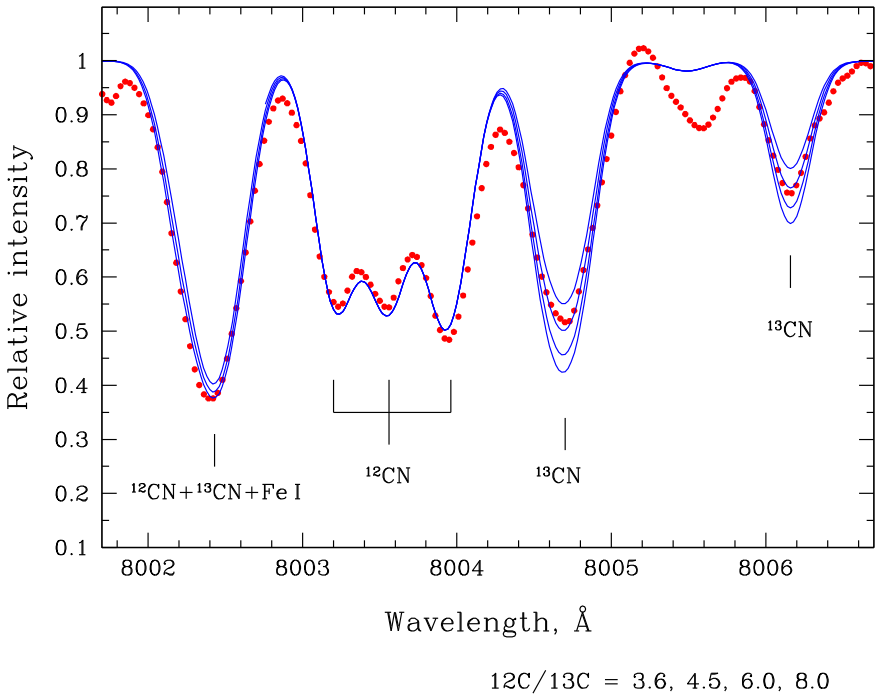

Figure 3. Observed (red dotted line) and synthetic (blue solid lines) spectra between 8002 Å and 8007 Å of StHα32. From top to bottom, we show the syntheses for the $^{12}C/^{13}C$ isotopic ratios of 3.6, 4.5, 6.0, and 8.0 for the carbon abundance of [C/Fe] = 0.67 and the nitrogen abundance of [N/Fe] = +0.99.

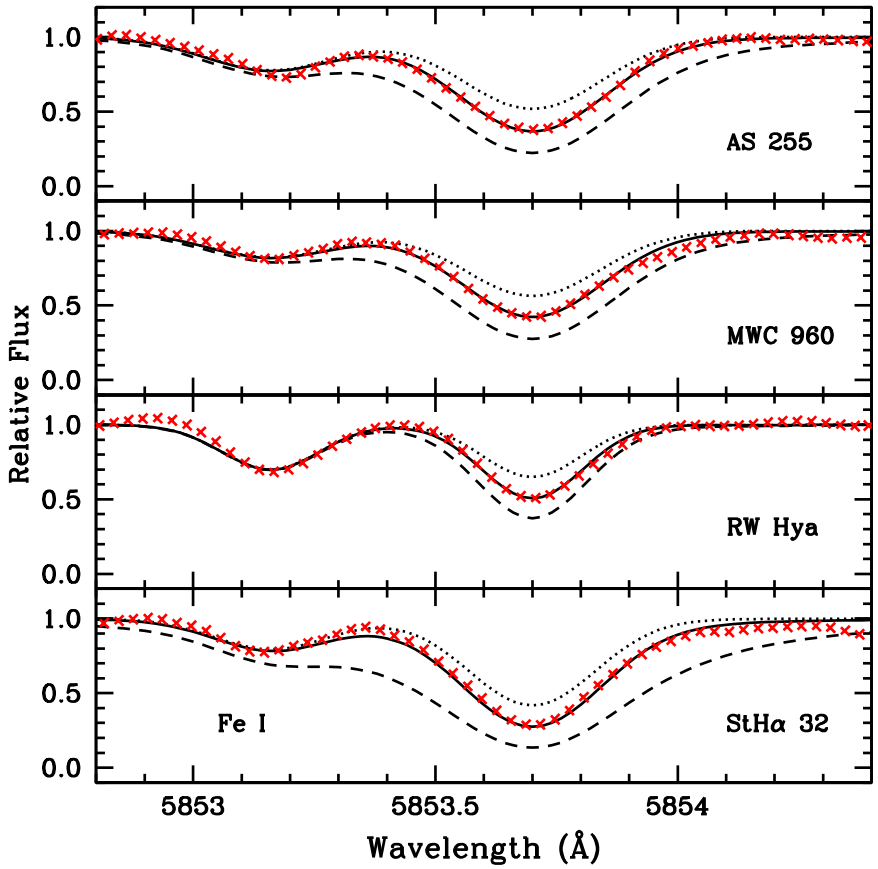

Figure 4. Observed (red dotted lines) and synthetic (black lines) spectra in the region around the Ba II line at 5853.69 Å. The solid black lines in the synthetic spectra show the adopted [Ba/Fe] ratio of +1.50 for AS 255, +1.42 for MWC 960, +0.02 for RW Hya, and +1.98 for StHα32. Dotted and dashed lines represent the synthetic spectra with [Ba/Fe] ratios of, respectively, −1.0 and +1.0 dex relative to the adopted abundance.

Table 6
Abundance Uncertainties for AS 255

Species	$\Delta T_{\rm eff}$ +130 K	$\Delta\log g$ +0.3	$\Delta\xi$ +0.3 km s^{-1}	Δ[Fe/H] +0.1	ΔW_λ +3 mÅ	$(\sum\sigma^2)^{1/2}$	$\sigma_{\rm obs}$
Fe I	+0.10	+0.05	−0.06	0.00	0.05	0.14	0.17
Fe II	−0.12	+0.21	−0.02	−0.02	0.06	0.25	0.10
Na I	+0.13	−0.02	−0.09	+0.01	0.03	0.16	⋯
Mg I	+0.04	+0.03	−0.04	0.00	0.04	0.07	⋯
Si I	−0.06	+0.09	−0.04	−0.02	0.04	0.12	0.19
Ca I	+0.16	−0.01	−0.12	+0.02	0.04	0.21	0.14
Ti I	+0.20	−0.02	−0.05	+0.01	0.03	0.21	0.12
Ni I	+0.09	+0.09	−0.02	−0.01	0.04	0.14	0.19
Y II	+0.01	+0.13	−0.17	−0.03	0.04	0.22	0.16
Zr I	+0.29	−0.01	−0.05	+0.02	0.03	0.30	0.20
Ba II	+0.03	+0.14	+0.14	−0.03	⋯	0.20	⋯
La II	+0.05	+0.15	−0.14	−0.03	0.04	0.22	0.11
Ce II	+0.03	+0.13	−0.12	−0.03	0.04	0.19	0.17
Nd II	+0.04	+0.13	−0.14	−0.03	0.04	0.20	0.13

Note. The second column gives the variation of the abundance ratios caused by the variation in $T_{\rm eff}$. The other columns give the variations due to $\log g$, ξ, [Fe/H], and W_λ, respectively. The seventh column gives the compounded rms uncertainty of the second to sixth columns. The last column gives the observed abundance dispersion of those elements with more than three available lines.

synthetic spectra in the region of the Fe I line at 6322.7 Å for AS 255 and MWC 960, the Fe I line at 6301.51 Å for StHα32 and the Ti I line at 6126.2 Å for RW Hya. We determined the rotational velocities using different lines because the symbiotic stars AS 255, MWC 960, and StHα32 have high radial velocities and some of the selected absorption lines are severely blended with telluric absorptions. For RW Hya, we used a different spectral region in order to avoid the TiO absorption bands.

Figure 5 shows the observed (red dots) and theoretical profiles that have been calculated for three $v \sin i$ values (from top to bottom): AS 255, 3.3 km s^{-1}, 6.3 km s^{-1} (adopted), and 9.3 km s^{-1}; MWC 960, 3.5 km s^{-1}, 6.5 km s^{-1} (adopted), and 9.5 km s^{-1}; StHα32, 2.5 km s^{-1}, 5.5 km s^{-1} (adopted), and 8.5 km s^{-1}; RW Hya, 2.8 km s^{-1}, 5.8 km s^{-1} (adopted), and 8.8 km s^{-1}. The typical uncertainty in the derived $v \sin i$ was 0.5–1.0 km s^{-1}. Following these rotational velocity determinations, we also determined the rotational velocities of five yellow symbiotic stars previously analyzed by Pereira & Roig (2009) and Pereira & Porto de Mello (1997): BD-21°3873, CD-43°14304, Hen 3-1213, Hen 3-863, and StHα176 whose values are 5.8 km s^{-1}, 8.5 km s^{-1}, 5.8 km s^{-1}, 9.0 km s^{-1}, and 3.0 km s^{-1}, respectively.

We see that the symbiotic stars analyzed in this work have lower rotational velocities than the values previously determined by Zamanov et al. (2007) who used Fourier cross-correlation technique. The strong blending of spectral lines in cool evolved stars, and in the symbiotic stars analyzed in this paper, may affect Fourier analysis for rotation, whereas matching of synthetic profiles to the observations permits to determine rotational velocities with high precision (Gray 2013). Our derived value of $v \sin i$ for RW Hya is in good agreement with the value obtained by Mikolajewska et al. (2014) of 6.3–6.6 km s^{-1}.

Based on our results, we obtained a mean value of 6.4 ± 2.0 km s^{-1} for the projected rotational velocities of yellow symbiotic stars, excluding StHα32 and RW Hya. Carlberg et al. (2011) obtained rotational velocities for single field giant stars. Excluding those at more than 1σ of their standard error, that is, those stars with rotational velocities higher than 9.0 km s^{-1}, which represents only 3% of their sample of 1288 stars, the mean rotational velocity of field giants is 4.5 ± 1.2 km s^{-1}. Clearly, yellow symbiotic stars rotate faster than single giants. It is important to determine rotational velocity, especially in the interacting binaries like symbiotic stars where the processes of mass transfer and accretion are taking place.

4.3. Evolutionary Status and Distances

4.3.1. RW Hya

To estimate the distances of the studied stars, we used the following relationship:

$$\log r\,(\mathrm{kpc}) = \frac{1}{2}\left(\log\frac{M_\star}{M_\odot} + 0.4(V - A_{\rm V} + BC) + 4\log T_{\rm eff} - \log g - 16.5\right) \quad (1)$$

where $T_{\rm eff}$ and $\log g$ are the effective temperature and the surface gravity previously determined, V is the visual magnitude, ($A_{\rm V}$) is the interstellar absorption, BC is the bolometric correction and $M_\star$ is the stellar mass.

Inserting the values of $T_{\rm eff} = 3900$ K and $\log g = 0.9$, and assuming for the mass $M = 1.6\,M_\odot$ (Schild et al. 1996) this equation becomes

$$5\log r\,(\mathrm{kpc}) = (V - A_{\rm V} + BC) - 7.58. \quad (2)$$

Considering $V = 9.0$ (Belczyński et al. 2000), $A_{\rm V} = 0.32$ (Mürset et al. 1991), and BC $= -1.16$, which is the bolometric correction given for the M giants (Houdashelt et al. 2000), Equation (2) gives $r = 1.23 \pm 0.39$ kpc considering the uncertainty of 0.2 dex in $\log g$ and 120 K in the temperature.

The bolometric magnitude resulting from the distance derived above is $M_{\rm bol\star} = -2.93$, and the luminosity is $\log(L_\star/L_\odot) = 3.07 \pm 0.30$ assuming $M_{\rm bol\odot} = +4.74$ for the Sun (Bessell et al. 1998), which is in good agreement with the value of $\log(L_\star/L_\odot) = 2.79 \pm 0.14$ obtained by Schild et al. (1996).

Using the values for the mass, effective temperature, and $\log g$ given in Mikolajewska et al. (2014), we obtain a distance

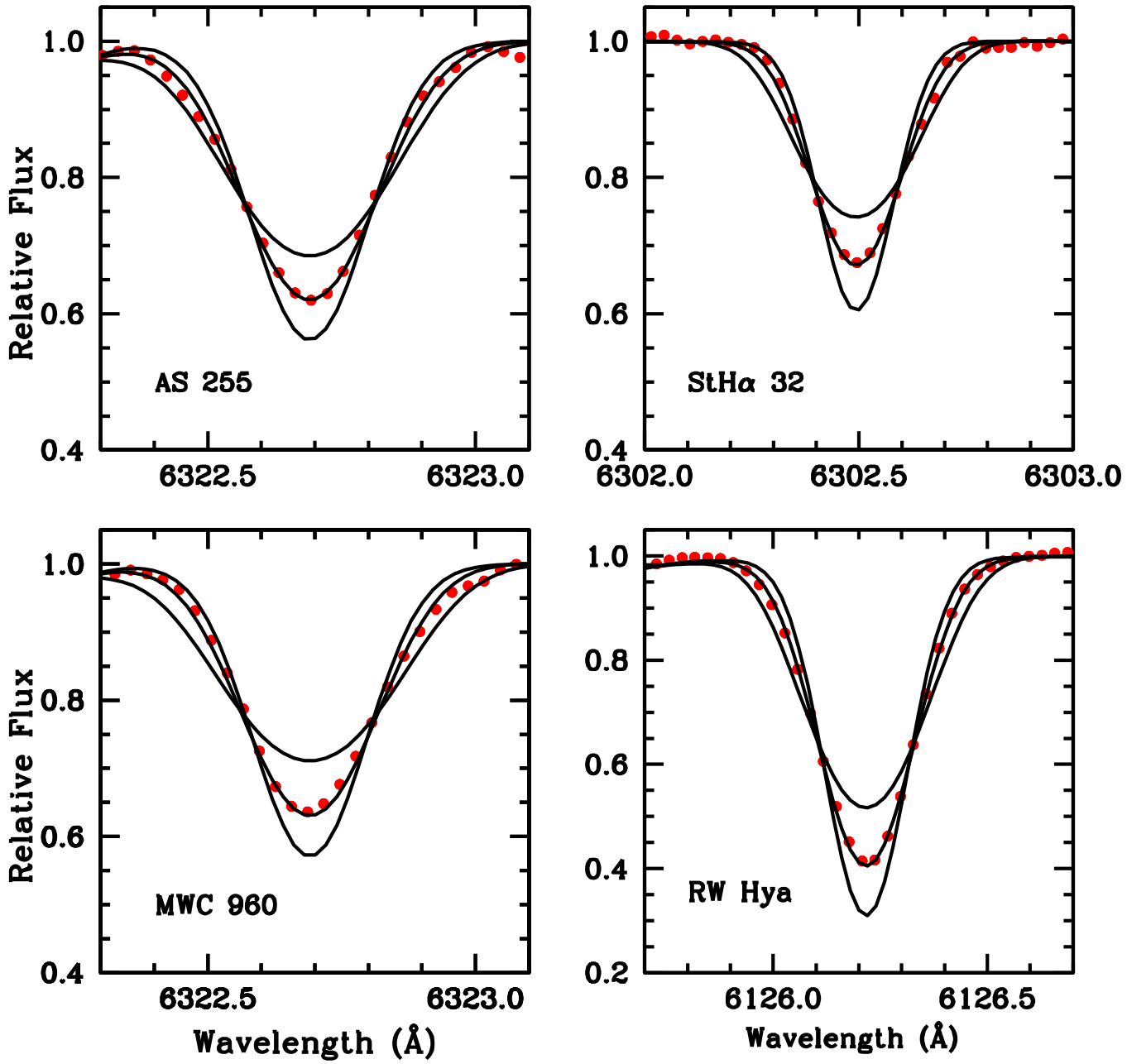

Figure 5. Observed (red dots) and synthetic spectra for the four symbiotic stars analyzed in this work. We show absorption profiles calculated with $v \sin i$ values derived in this paper (i) 6.3 km s^{-1} for AS 255; (ii) 6.5 km s^{-1} for MWC 960 in the region of the Fe I line at 6322.69 Å; (iii) 5.5 km s^{-1} for StHα32 in the region of the Fe I line at 6302.49 Å; (iv) 5.8 km s^{-1} for RW Hya in the region of the Ti I line at 6126.2 Å. The other synthetic spectra give the absorption profiles broadened by, respectively, −3.0 and +3.0 km s^{-1} of the adopted solution.

$r = 1.33 \pm 0.41$ kpc and a luminosity $\log(L_\star/L_\odot) = 3.37 \pm 0.35$, in good agreement with our derived values.

4.3.2. StHα32

For StHα32, inserting the values of $T_{\rm eff} = 4300$ K, $\log g = 1.1$ and assuming a mass $M_\star = 0.8\,M_\odot$ which is the most likely value for the mass of CH stars (McClure & Woodsworth 1990), BC = −0.66 as the bolometric correction given by Alonso et al. (1999) for giant stars with metallicity [Fe/H] = −1.3, and $A_V = 0.07$ based on the Galactic Dust Reddening and Extinction Service of IRSA, Equation (1) becomes

$$5 \log r\,(\rm kpc) = V - 8.64. \quad (3)$$

For the V-magnitude of StHα32, we consider the most recent value by Zacharias et al. (2013) and Henden et al. (2016) of 12.8 instead of 13.5 given in Belczyński et al. (2000) and obtain a distance r = 6.8 ± 2.0 kpc. The bolometric magnitude at that distance is $M_{\rm bol}\star = -2.09$, and the luminosity is $\log(L_\star/L_\odot) = 2.73 \pm 0.26$. This luminosity is not high enough to consider StHα32 as an AGB star that started helium shell burning and became self-enriched in neutron-capture elements. In fact, theoretical calculations show that for the first thermal pulse to develop, a star should have a luminosity of

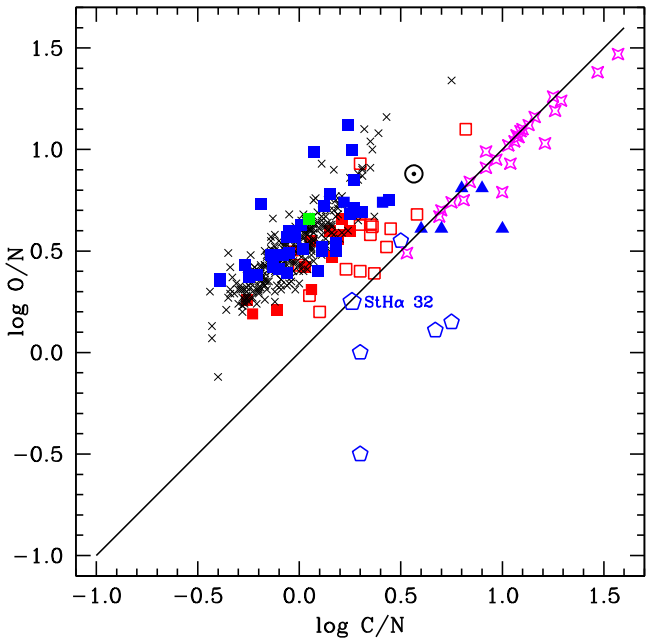

Figure 6. Relative abundance O/N vs. C/N. Disk carbon stars (magenta starry points); GK giants (black crosses); barium giants (red open squares); M giants (red filled squares); post-AGB stars enriched in the *s*-process elements (blue filled triangles); S-type symbiotics (blue filled squares); CH stars (blue open polygons). RW Hya is represented by a filled green square. StHα32 analyzed in this work is represented by a blue open polygon. Abundance data for barium giants are from Smith (1984), Barbuy et al. (1992), Allen & Barbuy (2006), Drake & Pereira (2008), and Sneden et al. (1981); M giants from Smith & Lambert (1985); CH stars from Vanture (1992b) and Pereira & Drake (2009); disk carbon stars from Lambert et al. (1986); GK giants from Luck & Heiter (2007); post-AGB stars from Van Winckel & Reyniers (2000), and S-type symbiotics including RW Hya from Galan et al. (2016, 2017).

$\log(L_\star/L_\odot) = 3.23$ ($M_{\rm bol} = -3.4$; Lattanzio 1986) or $\log(L_\star/L_\odot) = 3.14$ ($M_{\rm bol} = -3.1$; Vassiliadis & Wood 1993).

Since StHα32 displays properties of a halo star, such as high radial velocity and high Galactic latitude ($b = -30°$) and is also *s*-process enriched (Section 4.4.4), it is a CH star and hence a binary star. Indeed, according to Table 4 of Hartwick & Cowley (1985), CH stars have M_V values between −0.25 and −2.2. StHα32 with $M_V = -1.7$ is indeed a CH star.

4.3.3. AS 255 and MWC 960

For AS 255 and MWC 960, we do not provide estimates for distance and luminosity because the value of A_V, ≃1.5, which was used to place these two stars in the 2MASS diagram, is probably the maximum value for the interstellar reddening. In addition, the Na D_2 interstellar lines seen in the spectra of these two stars, which are useful to determine the amount of interstellar absorption, are strong and almost saturated (with equivalent widths higher than 1.0 Å) and/or present multiple components. This complicates the determination of the interstellar reddening based on the relationship between the equivalent widths of these lines and $E(B-V)$ given in Munari & Zwitter (1997).

4.4. Abundances

In the following, we will discuss the abundance pattern found in the four stars and compare it with previous studies of some stars in the thin disk, thick disk, and halo. We will also compare the heavy-element abundance pattern of these four stars with that of stars enriched in the *s*-process elements. Since we have determined the carbon abundance only for StHα32, we will discuss this result in comparison with other carbon abundance determinations for other evolved stars and chemically peculiar stars.

4.4.1. StHα32 in the log C/N – log O/N and $^{12}C/^{16}O - ^{12}C/^{13}C$ Diagrams

In Figure 6, we show the logO/N ratio versus the logC/N ratio for several classes of evolved stars and/or chemically peculiar objects for which CNO abundances have already been determined. The solid line represents the C/O = 1.0. In addition, the classical galactic carbon stars as well as the post-AGB stars were included in the diagram with the aim to show where the carbon-enriched objects are located, though the nitrogen abundances in the classical carbon stars should be observed with some caution (Lambert et al. 1986). Since barium stars (red open squares) are also giants but with some degree of carbon enrichment, their position in the logO/N versus logC/N diagram should not be the same as that of the non-enriched GK giants. The position of the S-type symbiotics (blue filled squares) is similar to the M-giants (red filled squares), which display nitrogen enrichment and are carbon underabundant.

For StHα32, we have log ϵ(C) = 7.81 and log ϵ(N) = 7.55. For the adopted metallicity for this star, [Fe/H] = −1.38, we obtain [C/Fe] = +0.67 and [N/Fe] = +1.01. For oxygen, because we have assumed [O/Fe] = +0.35, ϵ(O) = 7.80. Therefore, the position of StHα32 in Figure 6 is similar to that of the classical Galactic carbon stars (over to the C/O = 1.0 line), thus indicating that it is a carbon-rich object. Other carbon-enriched CH stars display lower (or lie in the lower limit of the) C/N ratio than classical Galactic carbon stars. In Figure 6, we also show the position of RW Hya (green square) analyzed in this work, for which the CNO abundances were obtained by Galan et al. (2016).

Abundance surveys for dwarf stars show that there is no trend for the [N/Fe] ratio versus [Fe/H] in the metallicity range between $-2.0 <$ [Fe/H] $< +0.3$, that is, [N/Fe] is ≈0.0 (Tomkin & Lambert 1984; Carbon et al. 1987). As the stars become giants, due to the deepening of their convective envelopes, nuclear processed material is brought from the interior to the outer layers of the stars changing the surface composition. As a consequence of the first dredge-up process, the abundance of ^{12}C is reduced and the abundance of nitrogen is enhanced (Lambert 1981); therefore, we should expect that the sum C+N should be conserved and [(C+N)/Fe] ∼ 0.0. In fact, in a sample of local giants analyzed by Luck & Heiter (2007), we found a mean value of 0.07 ± 0.06 for the [(C+N)/Fe] ratio. Single M giants analyzed by Smith & Lambert (1985, 1986) also have low values for the mean [(C+N)/Fe] ratio, that is 0.12 ± 0.09. Recently Galan et al. (2016) determined the abundances of carbon and nitrogen for a sample of 24 symbiotic stars. Using their values, we obtained a mean value of −0.03 ± 0.12. For CH stars, however, these values are higher. For a sample of seven CH stars, using the carbon and nitrogen abundances determined by Vanture (1992b), the mean [(C+N)/Fe] ratio is 1.13 ± 0.55 while for BD+04°2466, a CH star analyzed by Pereira & Drake (2009), we found 1.16. For StHα32, we found [(C+N)/Fe] = 0.87. These high values for the [(C+N)/Fe] ratio in CH stars and in StHα32 may be taken as evidence of the carbon enrichment due to mass transfer in the binary system.

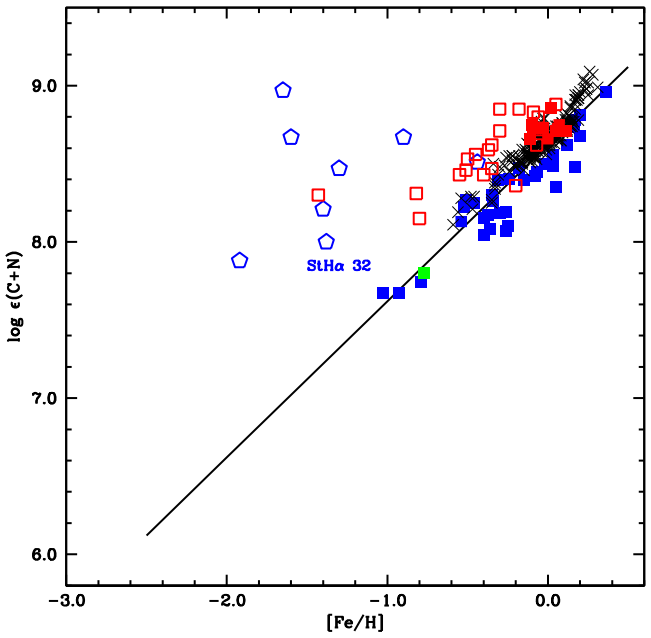

Figure 7. Observed C+N abundance in the notation of log ϵ(C+N). The solid line shows initial CN abundance for a given metallicity. Symbols have the same meaning as in Figure 6.

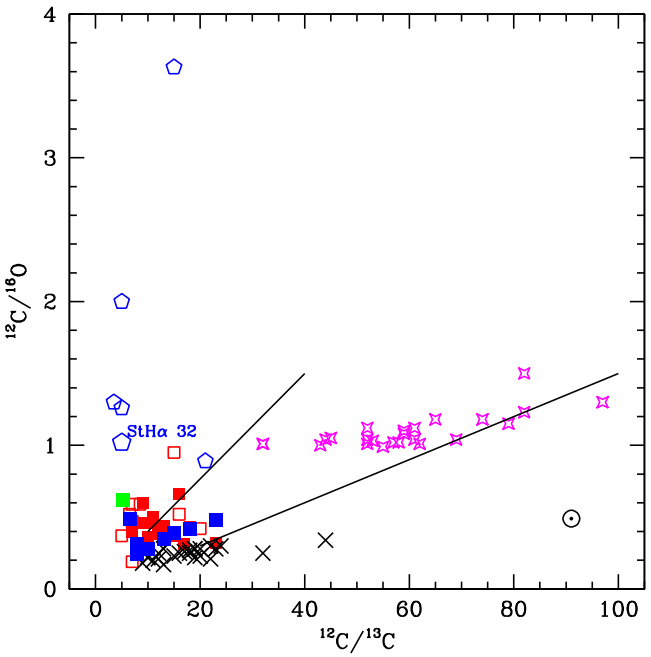

Figure 8. $^{12}C/^{16}O$ vs. $^{12}C/^{13}C$ ratios for several classes of stars and StHα32 analyzed in this work. Symbols have the same meaning as in Figure 6. The solid lines represent the addition of pure ^{12}C to $^{12}C/^{16}O$ and $^{12}C/^{13}C$ ratios.

Figure 7 provides further support that StHα32 is also carbon enriched, besides the nitrogen enrichment. The enhancement of carbon is due to mass transfer of the carbon-rich material from a former AGB star. From Figure 7, we see that StHα32 has a similar CN excess as seen in other CH stars, ~0.75. Figure 7 also shows that barium stars have a CN excess higher than the GKM giants and symbiotic stars.

In Figure 8, we show the $^{12}C/^{16}O$ versus $^{12}C/^{13}C$ for the same classes of stars shown in Figure 6, including StHα32. The two straight lines drawn according to Smith & Lambert (1990)

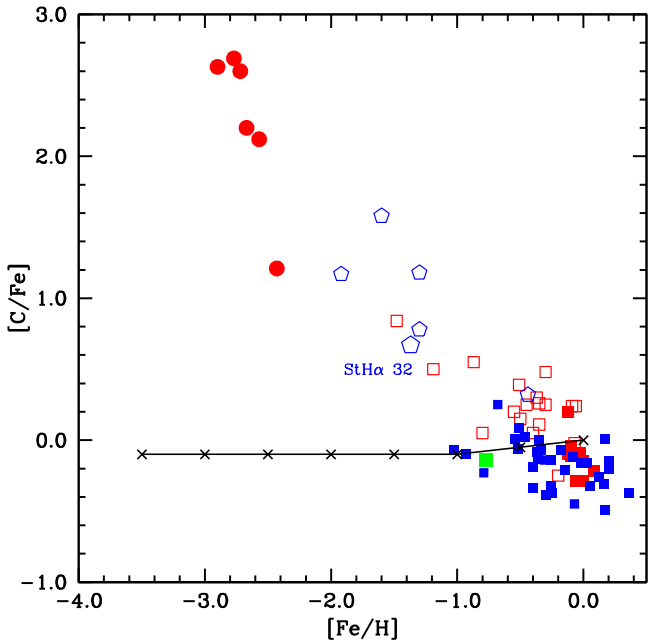

Figure 9. Diagram of [C/Fe] vs. [Fe/H]. Red filled circles represent binary CEMP-s stars with data taken from Hill et al. (2000), Lucatello et al. (2003), Sivarani et al. (2004), Barbuy et al. (2005), and Thompson et al. (2008). Other symbols have the same meaning as in Figure 6. The solid line is the mean [C/Fe] for field stars taken from Masseron et al. (2006).

represent the addition of ^{12}C material on the atmosphere of a star, one starting at ($^{12}C/^{13}C$, $^{12}C/^{16}O$) = (10, 0.4) and the other at ($^{12}C/^{13}C$, $^{12}C/^{16}O$) = (20, 0.3). According to these authors, an increase of ^{12}C by 2.5 times is necessary to change an M-type star to a C-type star, as expected by the third dredge-up. Then, these two straight lines represent the limits given by the distribution of M stars, where an addition of ^{12}C in their atmospheres would change them from oxygen-rich stars to carbon-rich stars. Barium stars (red open squares), M-giants (red filled squares), and S-type symbiotics (blue squares) occupy a region between the GK giants and C stars.

As the stars become giants, their mean $^{12}C/^{13}C$ ratio is 17.5 ± 0.21 (Lambert & Ries 1981), which is close to the predictions, 20–30 (Iben & Renzini 1983), considering the effects of the first dredge-up, which predicts nitrogen enrichment and a decrease of the $^{12}C/^{13}C$ ratio. In fact, these two abundance effects were not only observed in the GK giants, but also in M-giants (Smith & Lambert 1985), barium stars (Barbuy et al. 1992; Drake & Pereira 2008; Pereira & Drake 2009), and recently in cool M-type components of the S-type symbiotic stars (Galan et al. 2016). In CH stars, a low $^{12}C/^{13}C$ ratio (4−6) has already been found (Vanture 1992c) and StHα32 with a value of 5.0 also behaves like other stars with the same chemical peculiarity. It has already been claimed (Barbuy et al. 1992; Vanture 1992a) that the low $^{12}C/^{13}C$ ratio would be a result of two mixing episodes, the inversion of the mean molecular weight due to the accretion of carbon-rich material from the former AGB star on the binary system and, later, the occurrence of the first dregde-up.

4.4.2. StHα32 in the [C/Fe] - [Fe/H] Diagram

Like the [s/Fe] index (Section 4.3.4), the [C/Fe] ratio for the chemically peculiar objects, which are *s*-process enriched, is also anti-correlated with the metallicity. Figure 9 shows the [C/Fe] ratio plotted as a function of the metallicity. In fact,

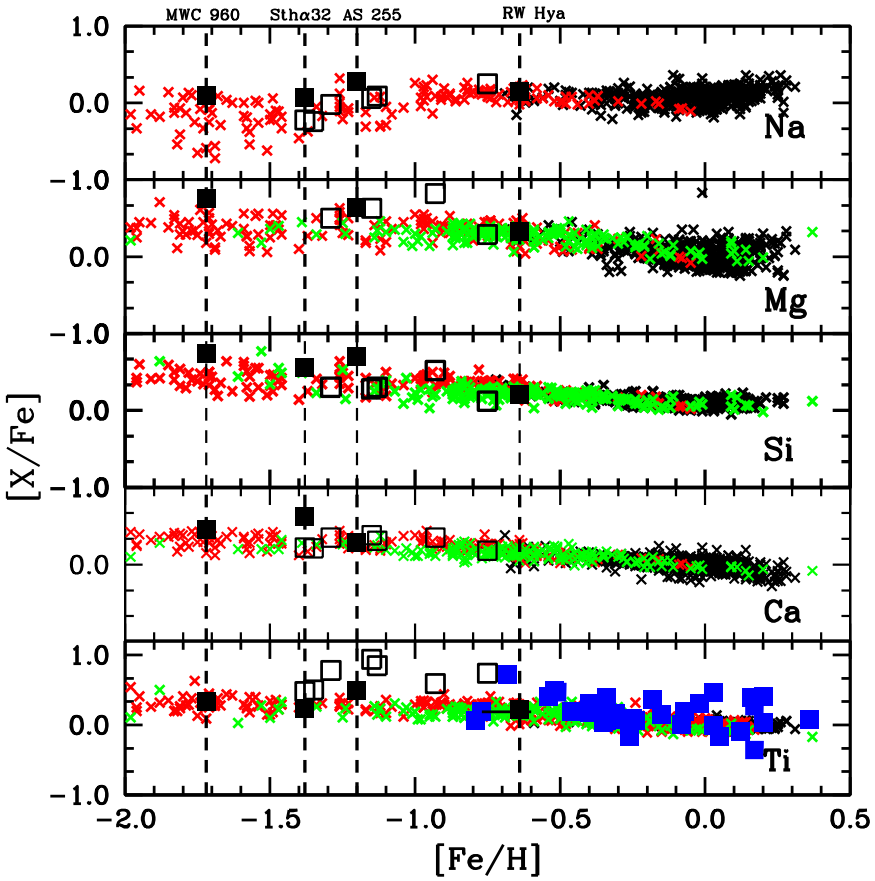

Figure 10. Abundance ratios [X/Fe] vs. [Fe/H] for Na, Mg, Si, Ca, and Ti. Symbiotic stars analyzed in this work (black filled squares); symbiotic stars previously analyzed by Pereira & Roig (2009; black open squares); field giants from Luck & Heiter (2007), Takeda et al. (2008), and Mishenina et al. (2006; black crosses); field giants analyzed by Fulbright (2000; red crosses); dwarf stars analyzed by Reddy et al. (2003, 2006; green crosses) and S-type symbiotics analyzed by Galan et al. (2016, 2017; blue filled squares). The horizontal solid line connects the [Ti/Fe] ratio determined in this work and in Galan et al. (2016).

such a trend was previously noted by Začs et al. (1998), Pereira & Drake (2009), and Masseron et al. (2006) for a sample of metal-poor carbon-rich stars, just to name a few. It is interesting that the [C/Fe] ratio in StHα32, a symbiotic star that hosts a CH star as the cool component of the system, also fits well into the trend seen in Figure 9 when compared with other binary and chemically peculiar stars.

4.4.3. Sodium to Nickel

Figures 10 and 11 show the abundance ratios [X/Fe] for sodium, α-elements (Mg, Si, Ca, and Ti), and nickel. The abundance ratios for these elements in the four symbiotic stars analyzed in this work are compared with previous studies done for the stars of the thin disk, thick disk, and halo. In addition, we also compared our results with previous analyses done for other symbiotic systems.

The abundance of sodium in dwarf thin disk and thick disk stars was determined by Reddy et al. (2003, 2006). In thin disk giant stars, sodium abundance was determined by Luck & Heiter (2007), Mishenina et al. (2006), and Takeda et al. (2008) and in the thick disk and halo by Fulbright (2000). In the disk and halo stars, sodium shows the same trend, basically $\langle$[Na/Fe]$\rangle = 0.00$; however, some stars in the halo show a sodium underabundance. The symbiotic stars analyzed in this work follow the same trend as seen in giants of similar metallicity.

The abundance of the α-elements (Mg, Si, Ca, and Ti) for the four symbiotic stars analyzed here also follows the same trend as that seen for the disk stars and halo stars, that is, α-elements show enhanced [X/Fe] ratios in the three low-metallicity stars of this sample. The iron group element nickel follows iron, therefore the [Ni/Fe] ratio remains constant near 0.0 for the stars of the thin disk, thick disk, and halo as well as the symbiotic stars of this study.

4.4.4. *s*-process Elements

Figures 11 and 12 show abundance ratios for the elements created by the *s*-process. Again, we compare our derived abundances with previous studies done for field giants and dwarfs of the disk, thick disk, and halo. As we can see in Figure 11, the abundance of zirconium is poorly investigated in normal giant stars in this metallicity range and lanthanum was only investigated for the local field giants, that is, in disk giant stars. Yttrium and barium are well covered in this broad metallicity range seen in Figures 11 and 12. The last panel of Figure 12 shows the [s/Fe] ratio for the field stars and the symbiotic stars. By [s/Fe], we mean the mean abundance ratio of the *s*-process elements ([Y/Fe], [Zr/Fe], [Ba/Fe], [La/Fe], [Ce/Fe], and [Nd/Fe]). For RW Hya, due to strong molecular opacity of the TiO bands, we were only able to determine the abundances of Zr, Ba, and Nd in some spectral regions free of the molecular lines.

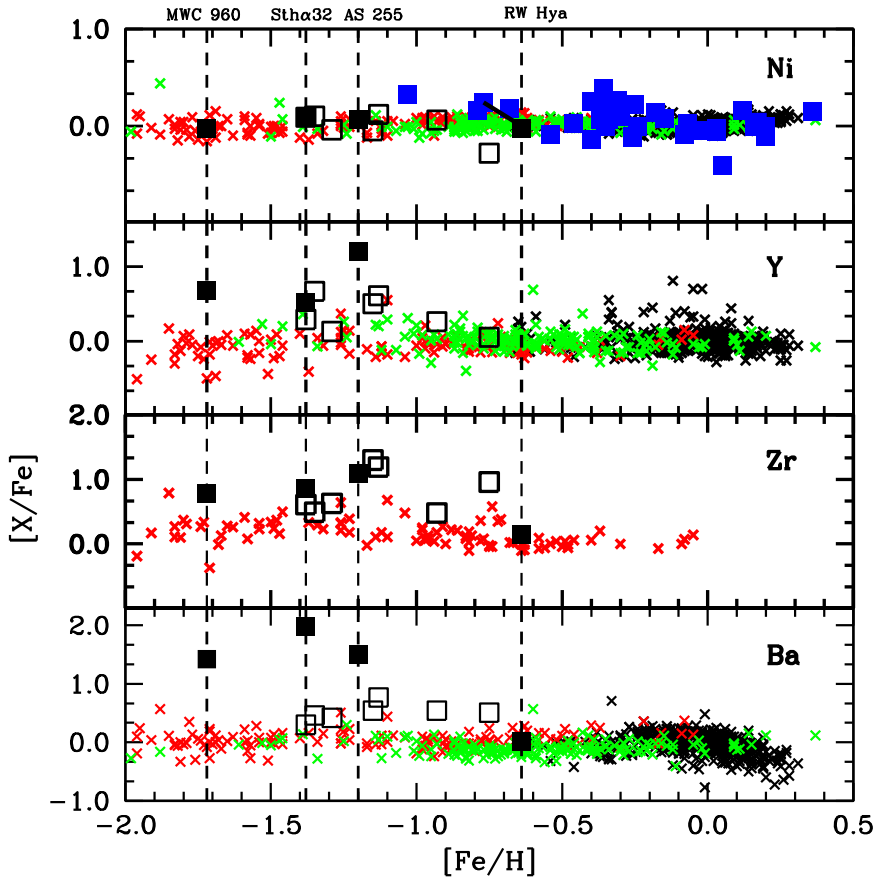

Figure 11. Abundance ratios [X/Fe] vs. [Fe/H] for Ni, Y, Zr, and Ba. Symbols have the same meaning as in Figure 10. Data for the field giants, dwarfs, and symbiotics are the same as in Figure 10. Additional abundance ratios for the *s*-process elements in field giants were taken from Mishenina et al. (2007). The solid line connects the [Ni/Fe] ratio determined in this work and in Galan et al. (2016).

Models of Galactic chemical evolution do not predict the observed overabundances of the *s*-process elements seen in Figures 11 and 12 for the stars AS 255, MWC 960, and StHα32 (Travaglio et al. 1999, 2004). Therefore, the atmospheres of these stars were contaminated either by any intrinsic process, such as a self-enrichment, or by an extrinsic event that may have happened in the past, i.e., mass transfer. As seen in Section 4.2, StHα32 is not luminous enough to be considered an AGB star and, therefore, it owes its *s*-process overabundance to the former AGB star. For RW Hya, we will discuss the abundances of the *s*-process elements in the next section. For AS 255 and MWC 960, although we could not derive their luminosities, we assumed that the *s*-process overabundances are the result of the mass transfer, like in other yellow-type symbiotics previously analyzed (Pereira & Roig 2009).

Figure 13 shows the abundance ratios [s/Fe] and [hs/ls] versus metallicity for a sample of 182 barium stars analyzed by de Castro et al. (2016; red squares), CH stars (blue pentagons), CEMP-s (Carbon Enhanced Metal-Poor) binary stars (red circles), two yellow symbiotics analyzed in this work (AS 255 and MWC 960) and the CH symbiotic star StHα32 (black filled squares), and the previously investigated yellow symbiotic stars (black open squares). The ratio [hs/ls], a useful measurement of the neutron-capture efficiency, has been widely used in the studies of AGB nucleosynthesis, and is defined as [hs/ls] = log $(\mathrm{hs/ls})_{\star}$/log $(\mathrm{hs/ls})_{\odot}$ where [hs] and [ls] are the mean abundance ratios of the s-elements at the Ba peak (Ba, La, Ce, and Nd) and Zr peak (Y and Zr). Figure 13 also shows the linear least-squares fits for the sample of barium stars and yellow symbiotic stars, for both [s/Fe] and [hs/ls] ratios versus metallicity. StHα32 was not included because it is a CH star, and barium stars with metallicities down to [Fe/H] < -1.0 were also excluded due to a small number of points.

For the thin and thick disk barium stars, the linear least-squares fits for [hs/ls] versus metallicity and [s/Fe] versus metallicity is [hs/ls] = $(0.09 \pm 0.03)-(0.80 \pm 0.10) \times$ [Fe/H] and [s/Fe] = $(0.72 \pm 0.04)-(0.75 \pm 0.15) \times$ [Fe/H] and for the yellow symbiotic stars (excluding StHα 32) the linear least-square fits are [hs/ls] = $(-0.26 \pm 0.27)-(0.39 \pm 0.22) \times$ [Fe/H] and [s/Fe] = $(0.23 \pm 0.57)-(0.49 \pm 0.46) \times$ [Fe/H], showing a larger scatter than for the barium stars. Both barium stars and yellow symbiotics (though being a smaller sample), two classes of objects of different stellar populations, display the same behavior as far as the nucleosynthesis of the *s*-process elements is concerned: both [hs/ls] and [s/Fe] ratios increase with decreasing metallicity. This is a consequence of the operation of the reaction ^{13}C(α, n)^{16}O, since this neutron source is anti-correlated with metallicity (Clayton 1988; Wallerstein 1997).

In fact, models from Busso et al. (2001), which provide the run of the [hs/ls] ratio with metallicity for a 1.5 $M_{\odot}$ and a 3.0 $M_{\odot}$ AGB star for different choices of ^{13}C pocket, show that the [hs/ls] ratio is anti-correlated with metallicity. Cristallo et al. (2011) included in the nucleosynthesis models the influence of the stellar mass on the [hs/ls] ratio. Goriely &

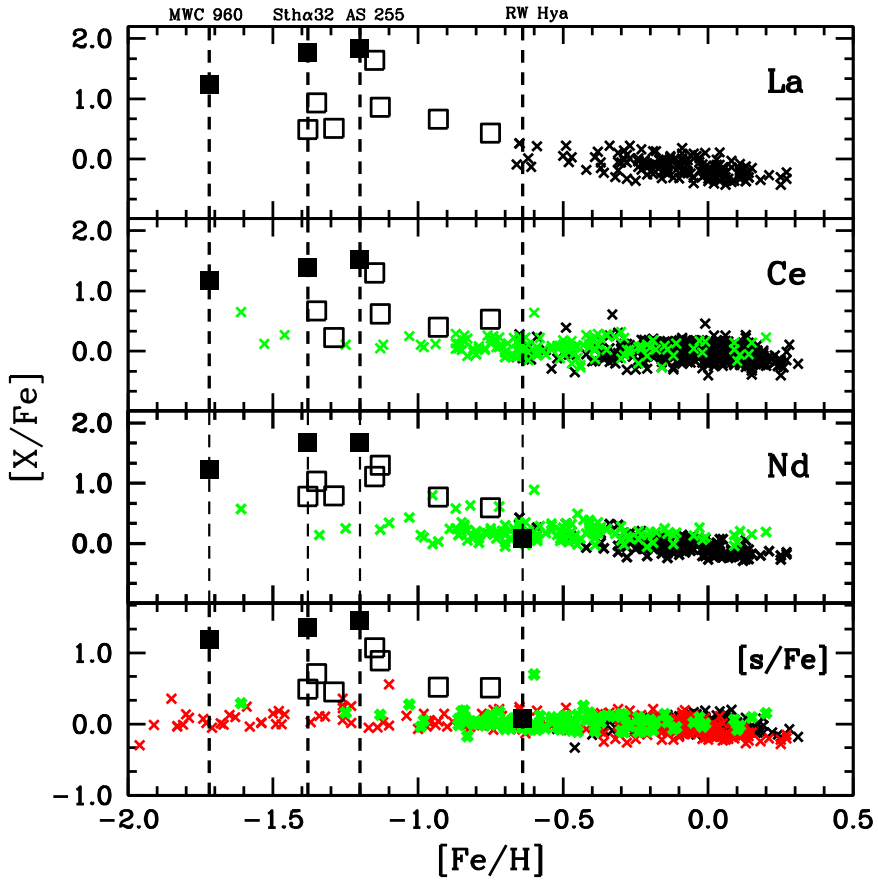

Figure 12. Abundance ratios [X/Fe] vs. [Fe/H] for La, Ce, Nd, and [s/Fe]. Symbols have the same meaning as in Figure 10. Data for field giants, dwarfs, and symbiotics are the same as in Figures 10 and 11.

Mowlavi (2000) showed that the negative values of the [hs/ls] ratio are expected for metallicities higher than −0.2 and positive values are seen up to metallicities around −0.6. From the above references, we can see the different ways by which the stellar masses and/or the number of thermal pulses are related to the [hs/ls] ratio, but the same general behavior with the metallicity is found in all the models.

Finally, it is worth mentioning that these ratios, [hs/ls] and [s/Fe], also provide important constraints not only for the nucleosynthesis models (number of thermal pulses of the former AGB star, the efficiency of thermal pulses) but also for the mass-transfer phenomenon in these binary systems (orbital separation, dilution factors, the way the matter was transferred from the AGB star: wind accretion in a detached binary system or by Roche lobe overflow; Jorissen et al. 1998; Liang et al. 2000; Lugaro et al. 2004).

To summarize this section, the abundances of the two yellow symbiotic stars and the CH symbiotic star analyzed in this work display the same pattern as observed in the other yellow symbiotics analyzed so far; low metallicity and overabundances of *s*-process elements with respect to stars of the same metallicity. StHα32 displays the highest value of the [hs/ls] ratio of the symbiotic stars studied in this work and its value is similar to that of other CH stars. As far as RW Hya is concerned, it also displays similar abundance ratios of stars with similar metallicity. However, its heavy-element abundance pattern does not show any significant enrichment and possible reasons for that are discussed in the next section.

4.4.5. Zr, Ba, and Nd in RW Hya

In the previous section, we mentioned that RW Hya is not enriched in the elements created by the *s*-process considering our temperature, surface gravity, and metallicity. We now consider whether this conclusion is related to the stellar parameters obtained by us. To check that, we determined the abundances of the elements of the *s*-process using the atmospheric parameters determined by Mikolajewska et al. (2014). Using their results, we found that the ratios [Zr/Fe], [Ba/Fe], and [Nd/Fe] have values of −0.26, −0.50, and −0.29, respectively. Therefore, our conclusion that RW Hya is not *s*-process enriched is not related to the derived atmospheric parameters.

Since RW Hya has been considered in the literature as an M-type symbiotic star, i.e., a red symbiotic star, the question regarding why red symbiotics do not exhibit enhancements of elements created by the *s*-process has already been raised in the literature. Jorrisen (2003) noticed the absence of extrinsic S stars among the red symbiotics. One of the reasons would be the high metallicity of some red symbiotics. The suspected high metallicity of red symbiotics was earlier considered by Whitelock & Munari (1992) because their infrared colors were similar to those of bulge M giants. This led these authors to conclude that, like the bulge giants, red symbiotic stars would also be high metallicity objects. In addition, if the red symbiotics were indeed high metallicity objects, their overabundances (if any) would not be detected since the efficiency of the *s*-process is anti-correlated with metallicity in systems

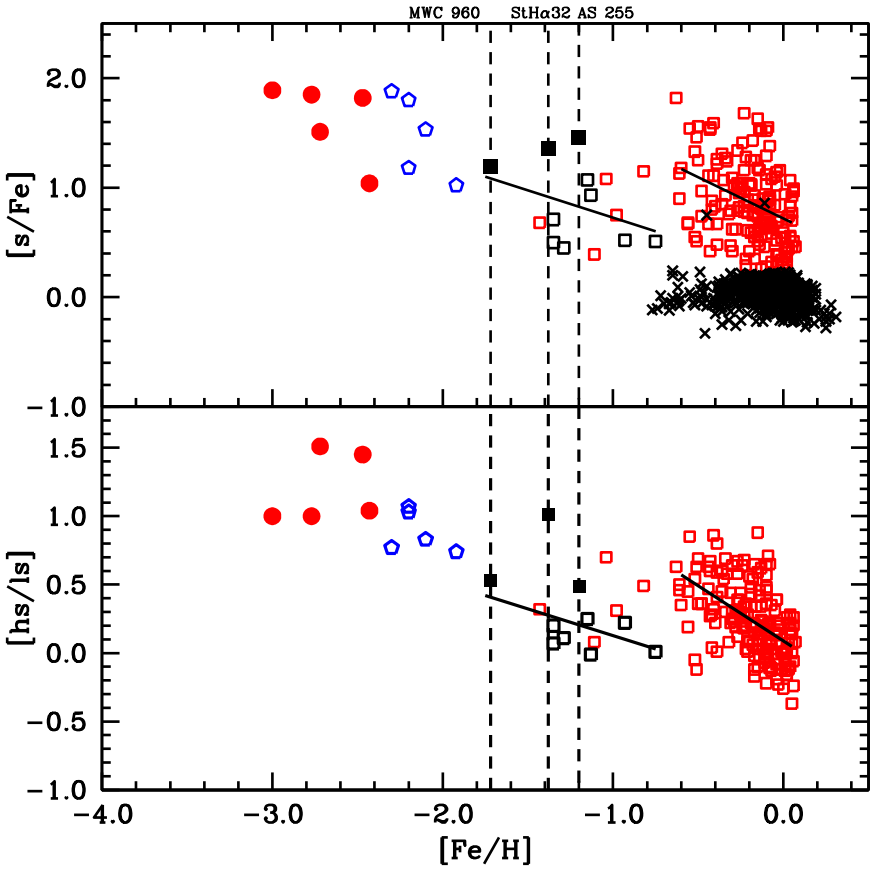

Figure 13. Diagram of [s/Fe] vs. [Fe/H] (top) and [hs/ls] vs. [Fe/H] (bottom) for several classes of chemically peculiar binary stars. Red filled circles represent the binary CEMP-s stars. Blue polygons represent the CH stars. We also show the least-square fits for [s/Fe] and [hs/ls] vs. [Fe/H] for the sample of barium stars (red open squares with data taken from de Castro et al. 2016) and yellow symbiotic stars. The CH symbiotic star StHα 32 was not included to obtain the least-square fits.

where the neutron source is the reaction $^{13}C(\alpha, n)^{16}O$ (Busso et al. 2001). In fact, the efficiency of the *s*-process, as given by the ratio [hs/ls] in systems with metallicities higher than the solar, has negative values, thus indicating a more efficient production of the lighter elements of the *s*-process compared to the heavier elements as it was shown in Pereira et al.'s (2011) study of the metal-rich barium stars. In that study, the authors also showed that the investigated stars have s-element enhancement factors, given by the ratio [s/Fe], between +0.25 and +1.16, thus indicating that even at high metallicities, it is possible to detect and to measure overabundances of the *s*-process elements if such overabundances are present. Another point to consider is whether red symbiotic stars have higher metallicities. New recent infrared high-resolution spectroscopic observations of a sample of 35 red symbiotic stars analyzed by Galan et al. (2016, 2017), showed that many stars do not display higher metallicities as was earlier suspected. We obtained a mean metallicity of -0.19 ± 0.35 (excluding the yellow symbiotic stars Hen 3-1213 and CD-43°14304 and including RW Hya analyzed by Mikolajewska et al. 2014).

Since we can rule out the suspected high metallicity of the red symbiotics as a possible explanation for the absence of *s*-process enrichment in these stars, two other possibilities remain: (i) the hot companion is a main-sequence star with an accretion disk instead of a white dwarf or (ii) the former AGB star does not passed through the TP-AGB phase (Jorrisen 2003). In fact, what these two possibilities are indeed considering is whether red symbiotics are pre-mass-transfer objects or post-mass-transfer systems (Jorissen et al. 2009). Jorissen et al. (2009) also discuss these two possibilities for the red symbiotics. The first possibility can be ruled out since there is no evidence of an accretion disk in RW Hya, based on the ultraviolet continuum (Sion et al. 2017). If the red symbiotics are indeed post-mass-transfer systems, one possible explanation for the absence of the overabundances of the *s*-process elements is that the evolved companion did not pass through the TP-AGB phase.

Another possibility that we would like to raise is whether dilution effects could be responsible for the absence of the overabundances of the *s*-process elements in symbiotic stars like RW Hya, if they are post-mass-transfer systems. In D′-type symbiotics (Smith et al. 2001; Pereira et al. 2005) and in a small number of planetary nebulae, such as Abel 35, LoTr 5 (Thévenin & Jasniewicz 1997), WeBo 1 (Bond et al. 2003), and Hen 2-39 (Miszalski et al. 2013), the combination of fast rotation and the observed overabundances of the elements of the *s*-process is currently explained by a companion star that accretes matter from the AGB wind (which is now the white dwarf) and starts to spin up (Jeffries & Stevens 1996). Two planetary nebulae escape the trend for these rapid rotators, Me 1-1 (Pereira et al. 2008) and LoTr 1 (Tyndall et al. 2013). These two planetary nebulae are indeed fast rotators but are not *s*-process enriched. In Pereira et al. (2008), the absence of the *s*-process overabundance was explained due to dilution effects by the deepening of the convective envelope. All red symbiotics, including RW Hya, have temperatures lower than 4000 K and many of them have masses between 1.0 and 2.0 $M_{\odot}$ (Mikolajewska 2003; Brandi et al. 2005; Zamanov et al. 2007; Galan et al. 2016). Therefore,

the accreted matter would be significantly diluted in the low-mass evolved stars, as they evolve from the main sequence to the red giant phase, and like Me 1-1 and LoTr 1, where no *s*-process overabundance was detected. Finally, we should consider another reason raised by Jorissen et al. (2009) to explain why these objects are not *s*-process enriched. Since red symbiotics and non-*s*-process enriched post-AGB stars share the same position in the (e–log P) diagram, both evolved types did not evolve in the AGB phase and develop thermal pulses to become self-enriched in the elements created by the *s*-process.

As far as the LoTr 1 is concerned, Tyndall et al. (2013) considered that this binary system had a different evolution as compared to systems like WeBo 1, due to their different nebular morphology. This would imply a different evolution for LoTr 1 with consequences for the mass of the progenitor or the amount of transferred mass.

5. Conclusions

The abundance analysis of three distinct types of symbiotic stars analyzed in this work, the two yellow symbiotic stars AS 255 and MWC 960, the CH symbiotic star StHα32, and the red symbiotic star RW Hya, employing high-resolution optical spectra, have revealed that AS 255, MWC 960, and StHα32 are enriched in *s*-process elements and that StHα32 is also carbon enriched. RW Hya is not enriched in the *s*-process elements. The abundance pattern of the α-group elements (Figure 10) follows the abundance pattern seen in the stars of the thick disk and halo. The metallicities of RW Hya and StHα32 also indicate that they should belong to the thick disk and halo population, respectively. In fact, using the distances obtained for RW Hya and StHα32, the radial velocities, and the proper motion data, we calculated that RW Hya has a probability of 98% of being a member of the thick disk and StHα32 has a probability of 99% of being a member of the halo. In these calculations, we followed the same procedure as was done in de Castro et al. (2016) and the data for proper motion for RW Hya were taken from Hög et al. (2000) and for StHα32 from Smart (2015).

For AS 255 and MWC 960, the stellar population these stars belong to is more difficult to address because of their low Galactic latitudes and longitudes within $\pm 10^{\circ}$ of the bulge. Apart from that, they share the same characteristics of the yellow symbiotics seen in the halo: low metallicity, enhanced α-elements, and, in some cases, high radial velocities. All of these characteristics have already been found in stars toward the bulge (De Propris et al. 2014; Koch et al. 2016). AS 255 has already been considered as a symbiotic star in the bulge by Medina Tanco & Steiner (1995). Ap 1-9 is another yellow symbiotic star considered to be a bulge symbiotic and also analyzed by Medina Tanco & Steiner (1995). Following the criterium given by Medina Tanco & Steiner (1995) to consider symbiotic stars in the bulge as those that have $(l^2 + b^2)^{1/2} \leqslant 20^{\circ}$, other yellow symbiotics besides AS 255 and Ap 1-9, also satisfy this criterium, such as MWC 960, V2905 Sgr, SS73-129, and probably Hen 3-1213. Hen 3-1213 marginally follows the criterium since it has $(l^2 + b^2)^{1/2} = 27^{\circ}$ but given its low galactic latitude and a high reddening of $A_V = 3.9$ it could probably be another symbiotic toward the bulge.

Since we do not have any information about the distances and reliable Galactic orbits of AS 255 and MWC 960, we considered that we should follow the same care as that raised in Koch et al. (2016). In that study, the authors consider that their sample stars toward the bulge could in fact be inner halo stars with an abundance pattern of the halo stars. The other yellow symbiotic stars Ap 1-9, SS73-129, and V2905 Sgr should also be observed with high resolution to check whether or not they display similar metallicity, abundance patterns, and radial velocities as the other yellow symbiotic stars. Assuming that they are bulge stars, a "standard" distance of 8.5 kpc will probably lead us to erroneous conclusions about their population, as raised by Koch et al. (2016).

As far as RW Hya is concerned, we raised two new discussions: (i) the first one concerns its position in the 2MASS diagram, which suggests that RW Hya may be an object at an intermediate position between the yellow and the red symbiotics. In this respect, it would be of great interest to obtain a high-resolution spectrum of SS 383, to check whether this object has a similar effective temperature and metallicity as RW Hya; and (ii) we discuss whether the absence of overabundance of the elements created by the *s*-process is due to dilution effects; this may set another constraint for theoretical models for the mass transfer in chemically peculiar binary stars and symbiotic stars as well.

Finally, we also determined the rotational velocities of the yellow symbiotic stars analyzed in this work and of other yellow symbiotic stars previoulsy analyzed. Although our sample is smaller than that of field giants analyzed by Carlberg et al. (2011), we showed that yellow symbiotic stars rotate faster than single giants. It will be important to further extend the determination of rotational velocities not only to other types of symbiotic stars but also to other classes of chemically peculiar binary stars, such as barium and CEMP stars. The rotational velocity would be another physical parameter that can be used to constrain the formation and evolution of binary systems.

L.F.M. acknowledges partial support from Spanish MINECO grant AYA2014-57369-C3-3-P (co-funded by FEDER funds). N.A.D. acknowledges FAPERJ, Rio de Janeiro, Brazil, for Visiting Researcher grant E-26/200.128/2015 and the Saint Petersburg State University for research grant 6.38.335.2015.

References

Allen, D. A. 1982, in Proc. Astrophys. Spa. Sci. Library 95, The Nature of Symbiotic Stars, ed. M. Friedjung & R. Viotti (Dordrecht: Reidel), 27
Allen, D. A., & Glass, I. S. 1974, MNRAS, 167, 337
Allen, D. A., & Glass, I. S. 1975, MNRAS, 170, 579
Allen, D. M., & Barbuy, B. 2006, A&A, 454, 895
Alonso, A., Arribas, S., & Martínez-Roger, C. 1999, A&AS, 140, 261
Antipova, L. I., Boyarchuk, A. A., Pakhomov, Yu. V., & Panchuk, V. E. 2004, ARep, 48, 597
Baella, N. O., Pereira, C. B., & Miranda, L. F. 2013, AJ, 146, 115
Baella, N. O., Pereira, C. B., Miranda, L. F., & Alvarez-Candal, A. 2016, AJ, 151, 100
Barbuy, B., Jorissen, A., Rossi, S. C. F., & Arnould, M. 1992, A&A, 262, 216
Barbuy, B., Spite, M., Spite, F., et al. 2005, A&A, 429, 1031
Belczyński, K., Mikonajewska, J., Munari, U., Ivison, R. J., & Friedjung, M. 2000, A&AS, 146, 407
Bessell, M. S., Castelli, F., & Plez, B. 1998, A&A, 333, 231
Bilir, S., Ak, S., Karaali, S., et al. 2008, MNRAS, 384, 1178
Bond, H. E., Pollacco, D. L., & Webbink, R. F. 2003, AJ, 125, 260
Brandi, E., Mikolajewska, J., Quiroga, C., et al. 2005, A&A, 440, 239
Busso, M., Gallino, R., Lambert, D. L., Travaglio, C., & Smith, V. V. 2001, ApJ, 557, 802
Carbon, D. F., Barbuy, B., Kraft, R. P., Friel, E. D., & Suntzeff, N. B. 1987, PASP, 99, 335
Carlberg, J. K., Majewski, S. R., Patterson, R. J., et al. 2011, ApJ, 732, 39
Castro, S., Rich, R. M., Grenon, M., Barbuy, B., & McCarthy, J. K. 1997, AJ, 114, 376
Cayrel, R. 1988, in IAU Symp. 132, The Impact of Very S/N Spectroscopy on Stellar Physics, ed. G. Cayrel de Strobel & M. Spite (Dordrecht: Kluwer), 345

Chen, Y. Q., Zhao, G., Nissen, P. E., Bai, G. S., & Qiu, H. M. 2003, ApJ, 591, 925
Clayton, D. D. 1988, MNRAS, 234, 1
Cristallo, S., Piersanti, L., Straniero, O., et al. 2011, ApJS, 197, 17
Cutri, R.M., Skrutskie, M.F., van Dyk, S., et al. 2003, The IRSA 2MASS All-Sky Point Source Catalog, NASA/IPAC Infrared Science Archive, yCat, 2246, 0
Davis, S. P., & Phillips, J. G. 1963, The Red System of the CN molecule (Berkeley, CA: Univ. California Press), 214
de Castro, D. B., Pereira, C. B., Roig, F., et al. 2016, MNRAS, 459, 4299
De Propris, R., Baldry, I. K., Bland-Hawthorn, J., et al. 2014, MNRAS, 444, 2200
Den Hartog, E. A., Lawler, J. E., Sneden, C., & Cowan, J. J. 2003, ApJS, 148, 543
Drake, J. J., & Smith, G. 1991, MNRAS, 250, 89
Drake, N. A., & Pereira, C. B. 2008, AJ, 135, 1070
Edvardsson, B., Andersen, J., Gustafsson, B., et al. 1993, A&A, 275, 101
Fluks, M. A., Plez, B., The, P. S., et al. 1994, A&AS, 105, 311
Fulbright, J. P. 2000, AJ, 120, 1841
Galan, C., Mikolajewska, J., Hinkle, K. H., & Joyce, R. R. 2016, MNRAS, 455, 1282
Galan, C., Mikolajewska, J., Hinkle, K. H., & Joyce, R. R. 2017, MNRAS, 466, 2194
Goriely, S., & Mowlavi, N. 2000, A&A, 362, 599
Gratton, R. G., & Sneden, C. 1988, A&A, 204, 193
Gray, D. F. 2013, AJ, 146, 29
Grevesse, N., & Sauval, A. J. 1998, SSRv, 85, 161
Gromadzki, M., Mikołajewska, J., & Soszyński, I. 2013, AcA, 63, 405
Hartwick, F. D. A., & Cowley, A. P. 1985, ApJ, 90, 2244
Henden, A. A., Templeton, M., Terrell, D., et al. 2016, yCat, 2336, 0
Hill, V., Barbuy, B., Spite, M., et al. 2000, A&A, 353, 557
Hög, E., Fabricius, C., Makarov, V. V., et al. 2000, A&A, 357, 367
Houdashelt, M. L., Bell, R. A., Sweigart, A. V., & Wing, R. F. 2000, AJ, 119, 1424
Iben, I., & Renzini, A. 1983, ARAA, 21, 271
Jeffries, R. D., & Stevens, I. R. 1996, MNRAS, 279, 180
Jorissen, A., Frankowski, A., Famaey, B., & van Eck, S. 2009, A&A, 498, 489
Jorissen, A., Van Eck, S., Mayor, M., & Udry, S. 1998, A&A, 332, 877
Jorrisen, A. 2003, in ASP Conf. Ser. 303 (San Francisco, CA: ASP), 25
Kaufer, A., Stahl, O., Tubbesing, S., et al. 1999, Msngr, 95, 8
Koch, A., McWilliam, A., Preston, G. W., & Thompson, I. B. 2016, A&A, 587, 124
Kurucz, R. L. 1993, CD-ROM 13, Atlas9 Stellar Atmosphere Programs and 2 km s^{-1} Grid (Cambridge: Smithsonian Astrophys. Obs) https://doi.org/10.1007/978-94-009-8492-9_10
Lambert, D. L. 1981, ASSL, 88, 115
Lambert, D. L., Gustafsson, B., Eriksson, K., & Hinkle, K. H. 1986, ApJS, 62, 373
Lambert, D. L., Heath, J. E., Lemke, M., & Drake, J. 1996, ApJS, 103, 183
Lambert, D. L., & Ries, L. M. 1981, ApJ, 248, 228
Lattanzio, J. C. 1986, ApJ, 311, 708
Lawler, J. E., Sneden, C., Cowan, J. J., Ivans, I. I., & Den Hartog, E. A. 2009, ApJS, 182, 51
Liang, Y. C., Zhao, G., & Zhang, B. 2000, A&A, 363, 555
Lucatello, S., Gratton, R., Cohen, J. G., Beers, T. C., & Christlieb, N. 2003, AJ, 125, 875
Luck, R. E., & Heiter, U. 2007, AJ, 133, 2464
Lugaro, M., Ugalde, C., Karakas, A. I., et al. 2004, ApJ, 615, 934
Martin, G. A., Fuhr, J. R., & Wiese, W. L. 1988, JPCRD, 17, 4
Masseron, T., van Eck, S., Famaey, B., et al. 2006, A&A, 455, 1059
McClure, R. D., & Woodsworth, A. W. 1990, ApJ., 352, 709
McWilliam, A. 1998, AJ, 115, 1640
Medina Tanco, G. A., & Steiner, J. E. 1995, AJ, 109, 1770
Mikolajewska, J. 2003, in ASP Conf. Ser. 303, Symbiotic Stars Probing Stellar Evolution, ed. R. L. M. Corradi, J. Mikolajewska, & T. J. Ma- honey (San Francisco, CA: ASP), 9
Mikolajewska, J., Galan, C., Hinkle, K. H., Gromadzki, M., & Schmidt, M. R. 2014, MNRAS, 440, 3016
Mishenina, T. V., Bienaymé, O., Gorbaneva, T. I., et al. 2006, A&A, 456, 1109
Mishenina, T. V., Gorbaneva, T. I., Bienaymé, O., et al. 2007, ARep, 51, 382
Miszalski, B., Boffin, H. M. J., Jones, D., et al. 2013, MNRAS, 436, 3068
Munari, U., & Zwitter, T. 1997, A&A, 318, 269
Mürset, U., Nussbaumer, H., Schmid, H. M., & Vogel, M. 1991, A&A, 248, 458
Mürset, U., & Schmid, H. M. 1999, A&AS, 137, 473
Pereira, C. B., & Drake, N. A. 2009, A&A, 496, 791
Pereira, C. B., Miranda, L. F., Smith, V. V., & Cunha, K. 2008, A&A, 477, 877
Pereira, C. B., & Porto de Mello, G. F. 1997, AJ, 114, 2128
Pereira, C. B., & Roig, F. 2009, AJ, 137, 118
Pereira, C. B., Sales Silva, J. V., Chavero, C., Roig, F., & Jilinski, E. 2011, A&A, 533, 51
Pereira, C. B., Smith, V. V., & Cunha, K. 1998, AJ, 116, 1977
Pereira, C. B., Smith, V. V., & Cunha, K. 2005, A&A, 429, 993
Pradhan, A., & Dalgarno, A. 1994, PhRvA, 49, 960
Reddy, B. E., Bakker, E. J., & Hrivnak, B. J. 1999, ApJ, 524, 831
Reddy, B. E., Lambert, D. L., & Allende Prieto, C. 2006, MNRAS, 367, 1329
Reddy, B. E., Tomkin, J., Lambert, D. L., & Allende Prieto, C. 2003, MNRAS, 340, 304
Ridgway, S. T., Joyce, R. R., White, N. M., & Wing, R. F. 1980, ApJ, 235, 126
Santrich, O. J. K., Pereira, C. B., & Drake, N. A. 2013, A&A, 554, 2
Schadee, A. 1964, BAN, 17, 311
Schild, H., Müerset, U., & Schmutz, W. 1996, A&A, 306, 477
Schmid, H. M. 1994, A&A, 284, 156
Schmid, H. M., & Nussbaumer, H. 1993, A&A, 268, 159
Sion, E., Godon, P., Mikolajewska, J., Sabra, B., & Kolobow, C. 2017, arXiv:1702.07341
Sivarani, T., Bonifacio, P., Molaro, P., Cayrel, R., & Spite, M. 2004, A&A, 413, 1073
Smart, R. L. 2015, yCat, 6145, 0
Smith, G., Edvardsson, B., & Frisk, U. 1986, A&A, 165, 126
Smith, V. V. 1984, A&A, 132, 326
Smith, V. V., Cunha, K., Jorissen, A., & Boffin, H. M. J. 1996, A&A, 315, 179
Smith, V. V., Cunha, K., Jorissen, A., & Boffin, H. M. J. 1997, A&A, 324, 97
Smith, V. V., & Lambert, D. L. 1985, ApJ, 294, 326
Smith, V. V., & Lambert, D. L. 1986, ApJ, 311, 843
Smith, V. V., & Lambert, D. L. 1990, ApJS, 72, 387
Smith, V. V., Pereira, C. B., & Cunha, K. 2001, ApJ, 556, L55
Sneden, C. 1973, PhD thesis, Univ. Texas
Sneden, C., & Lambert, D. L. 1982, ApJ, 259, 381
Sneden, C., McWilliam, A., Preston, G. W., et al. 1996, ApJ, 467, 819
Sneden, C., Pilachowski, C. A., & Lambert, D. L. 1981, ApJ, 247, 1052
Takeda, Y., Sato, B., & Murata, D. 2008, PASJ, 60, 781
Thévenin, F., & Jasniewicz, G. 1997, A&A, 320, 913
Thompson, I. B., Ivans, I. I., Bisterzo, S., Sneden, C., & Gallino, R. 2008, ApJ, 677, 556
Tomkin, J., & Lambert, D. L. 1984, ApJ, 279, 220
Travaglio, C., Galli, D., Gallino, R., et al. 1999, ApJ, 521, 691
Travaglio, C., Gallino, R., Arnone, E., et al. 2004, ApJ, 601, 864
Tyndall, A. A., Jones, D., Boffin, H. M. J., et al. 2013, MNRAS, 436, 2082
Van Winckel, H., & Reyniers, M. 2000, A&A, 354, 135
Vanture, A. D. 1992a, AJ, 103, 2035
Vanture, A. D. 1992b, AJ, 104, 1986
Vanture, A. D. 1992c, AJ, 104, 1997
Vanture, A. D., & Wallerstein, G. 2002, ApJ, 564, 395
Vassiliadis, E., & Wood, P. R. 1993, ApJ, 413, 641
Wallerstein, G. 1997, RvMP, 69, 995
Whitelock, P. A., & Munari, U. 1992, A&A, 255, 171
Wiese, W. L., Smith, M. W., & Miles, B. M. 1969, Atomic Transition Probabilities, Vol. 2 (Washington, D.C.: National Bureau of Standards)
Wyller, A. A. 1966, ApJ, 143, 828
Zacharias, N., Finch, C. T., Girard, T. M., et al. 2013, AJ, 145, 44
Zamanov, R. K., Bode, M. F., Melo, C. H. F., et al. 2007, MNRAS, 380, 1053
Začs, L., Nissen, P. E., & Schuster, W. J. 1998, A&A, 337, 216